

NOT FOR PUBLICATION
See note overleaf

AAEC/PR43-PD
INDC (AUL) -27/G



AAEC/PR43-PD
INDC (AUL) -27/G



XA04N2777

INIS-XA-N--165

AUSTRALIAN ATOMIC ENERGY COMMISSION

RESEARCH ESTABLISHMENT

LUCAS HEIGHTS

PROGRESS REPORT OF PHYSICS DIVISION

1st OCTOBER, 1976-30th SEPTEMBER, 1977

ACTING DIVISION CHIEF - MR. W. GEMMELL

NOT FOR PUBLICATION

This report was printed for circulation within the Australian Atomic Energy Commission. It has not been reviewed for general issue.

It is made available on the understanding that the information it contains will not be quoted in publications, listed in abstract journals or communicated to the press.

AUSTRALIAN ATOMIC ENERGY COMMISSION
RESEARCH ESTABLISHMENT
LUCAS HEIGHTS

PROGRESS REPORT OF PHYSICS DIVISION
1st OCTOBER, 1976-30th SEPTEMBER, 1977
ACTING DIVISION CHIEF - MR. W. GEMMELL

CONTENTS

	Page
1. INTRODUCTION	1
2. REACTOR STUDIES	2
2.1 Moata Operations	2
2.2 Reactor Physics Experiments	4
2.2.1 Critical Facility	4
2.3 Integral Pulsed Neutron Experiments with Heavy Metal Assemblies	4
2.4 Time-dependent Spectra in Heavy Metal Assemblies	7
2.5 Neutron Spectrometry	8
2.5.1 Neutron energy spectra from thick target Li(p,n)Be sources	8
2.6 Reactor Safety	8
2.6.1 LOCA analysis	8
2.6.2 Reactor transient studies	11
2.6.3 Transient boiling heat transfer	14
2.7 HIFAR	14
2.7.1 Reactor dynamics	14
2.8 Deep Ocean Currents and Disposal of Radioactive Waste into the Ocean	15
2.9 Applications	15
2.9.1 Thorium analysis by neutron activation and gamma spectrometry	15
2.9.2 Neutron moisture meter investigations	17
2.9.3 Pressure dependence of plasma formation under laser irradiation	18
2.10 Neutron Source Project	18
3. NEUTRON PHYSICS	19
3.1 3 MeV Van de Graaff Accelerator	19
3.2 Fission Studies	22
3.2.1 Collaboration with Bruyères-le-Châtel	22
3.2.2 Review of $\bar{\nu}$ values for thermal fission and ^{252}Cf	22
3.2.3 Revision of energy dependent $\bar{\nu}$ data for Pu isotopes	23
3.2.4 Measurement of the ^{252}Cf spontaneous fission neutron spectrum	23
3.2.5 Fission fragment angular distribution for ^{230}Th ^{232}Th	23
3.2.6 Measurement of fragment kinetic energies for $^{239}\text{Pu}(n,f)$	24
3.3 Neutron Capture Studies	25
3.3.1 Joint AAEC/ORNL nuclear data project	25
3.3.2 Resonance neutron capture systematics	25
3.3.3 Neutron sensitivity of capture γ -ray detectors	27
3.3.4 Radiative capture cross sections of ^{23}Na	29
3.3.5 Resonance neutron capture in Sc below 100 keV	29
3.3.6 Resonant and background interference in ^{54}Fe capture	29
3.3.7 Resonance parameters for ^{89}Y	32
3.3.8 Resonance parameters of ^{91}Zr and ^{96}Zr	32
3.3.9 Resonance parameters for the even-A isotopes of Cd	32

CONTENTS (cont'd)

	Page
3.3.10 Neutron capture in ^{139}La	34
3.3.11 Neutron capture in ^{138}Ba and ^{140}Ce	34
3.3.12 Gamma rays from keV neutron capture in lanthanum	34
3.3.13 Branching ratio of ^{176}Lu at astrophysical energies	36
3.3.14 Radiative capture cross section of ^{208}Pb	36
3.3.15 Neutron resonance spectroscopy on ^{209}Bi	39
3.3.16 s-wave neutron capture in ^{209}Bi	39
3.4 Nuclear Techniques of Analysis	41
3.4.1 New beam line facilities	41
3.4.2 Proton induced X-rays	41
3.4.3 Artefacts	44
3.4.4 Tin on glass	44
3.4.5 Aluminium	44
3.4.6 Oxygen	48
3.4.7 Surface fluorine layers	48
3.4.8 Minibeam	48
3.4.9 Gamma ray catalogue	48
3.4.10 Bibliography	48
4. THEORETICAL PHYSICS	50
4.1 AUS Modular Scheme	50
4.1.1 AUS module POW3D	50
4.1.2 Collision probability methods	50
4.1.3 Calculation of fast reactor benchmark experiments	50
4.2 Radiation Shielding	52
4.2.1 Bilinear vs. linear weighting of multigroup cross sections	52
4.2.2 Commissioning of DOT code	52
4.2.3 Overburden over ores	52
4.2.4 Neutron and gamma ray flux levels around SILOE	53
4.2.5 Safe calculations	53
4.3 Reactor Data	53
4.3.1 Fission product cross section library	53
4.3.2 Calculation of average reaction cross sections	54
4.3.3 Resonance parameter analysis	54
4.4 Other Items	55
4.4.1 Detector calculations	55
4.4.2 Magnetohydrodynamics and topping cycles	55
4.4.3 Inverse reaction problem	56
4.4.4 Applications of unfolding techniques	56
4.4.5 Flux spectrum unfolding	56
4.4.6 Interactive computing methods	57
4.5 Energy Systems Analysis	57
4.5.1 Australian energy data file	57
4.5.2 Australian usage of low grade heat to 200°C	58

CONTENTS (cont'd)

	Page
5. RUM JUNGLE ENVIRONMENTAL STUDIES	58
5.1 Field Measurements of Rainfall and Run-off	58
5.2 Rainfall Contribution to Ground Water	59
5.3 Model for Heap Leaching	59
6. PUBLICATIONS	60
6.1 Papers	60
6.2 Reports	61
6.3 Conference Papers	62
Table 2.1 Hot startup excursions	
Table 2.2 Hot standby and operating power excursions	
Table 3.1 Accelerator time allocation	
Table 3.2 Recommended \bar{v} values	
Table 3.3 Average resonance parameters for the cadmium isotopes	
Table 3.4 ^{208}Pb resonance parameters	
Table 3.5 Maxwellian averaged neutron capture by ^{208}Pb	
Table 3.6 Amended s-wave parameters for ^{209}Bi	
Table 3.7 Maxwellian averaged capture cross sections for ^{209}Bi	
Table 3.8 Proton induced gamma rays: thick sample yields	
Table 4.1 Fast reactor benchmark criticality	
Table 4.2 Theoretical estimate of levels missed	
Fig. 2.1 Development of beam seed root system: time lapsed neutron radiography	
Fig. 2.2 Time dependent ^{235}U reaction rates in depleted U assemblies	
Fig. 2.3 Instantaneous ^{235}U reaction decay rate in depleted U assemblies	
Fig. 2.4 Fundamental mode reaction rates - measured and calculated	
Fig. 2.5 Neutron yield at 0° from $\text{Li}(p,n)$ reaction	
Fig. 2.6 Mass of fluid in rig in first few seconds after blowdown	
Fig. 2.7 Time behaviour of blowdown pressure in semiscale experiment S-02-6	
Fig. 2.8 Peak power in SPERT III-E cold start up transient	
Fig. 2.9 Modelling of water cooled heater temperature transient	
Fig. 2.10 HIFAR power transient resulting from increased coolant flow	
Fig. 2.11 Gamma activity from thorium ore samples as function of thorium concentration	
Fig. 2.12 Plasma formation threshold as function of gas pressure	
Fig. 3.1 Correlation of valence and total radiative widths in 3s and 3p mass regions	
Fig. 3.2 Neutron sensitivity of gamma detector as function of neutron energy	
Fig. 3.3 Prompt background influence on symmetry of capture resonances	
Fig. 3.4 Asymmetric resonances: interference between valence channels and broad resonances	
Fig. 3.5 7.7 keV ^{54}Fe resonance fit and thermal background cross section	
Fig. 3.6 (a) p-wave strength functions for cadmium isotopes (b) s-wave strength functions for Zr, Cd, Te isotopes	
Fig. 3.7 Fit to a doublet at 68 keV and the 78 keV $1/2^-$ resonance in ^{208}Pb .	
Fig. 3.8 Fit to 500 keV dip in ^{208}Pb using $\Gamma_n = 60$ keV	

CONTENTS (cont'd)

- Fig. 3.9 Typical raw PIXE spectrum
- Fig. 3.10 PIXE spectrum using electron flood technique
- Fig. 3.11 Filtering of PIXE spectrum to remove sum peaks
- Fig. 3.12 Background removal and peak fitting analysis
- Fig. 3.13 S_n variation on glass as determined by alpha scattering
- Fig. 3.14 Yield of $^{27}\text{Al}(p,\gamma)^{28}\text{Si}$ reaction as function of energy and aluminium thickness

1. INTRODUCTION

The maturity of the nuclear industry is exemplified by the increasingly large effort required to improve upon existing levels of knowledge or understanding. Our experiment to provide an accurate measurement of the californium fission neutron spectrum has been delayed by the necessity to investigate the many small correction effects and validate the new features introduced. The same type of painstaking analysis has become necessary in the collaborative studies with Oak Ridge National Laboratory on neutron capture cross sections. Investigation of background, interference and experimental techniques has led to significant revisions of the data and, again, emphasises the care necessary before such data becomes incorporated into international data collections.

A continuing worry in all of this is the adequacy of our major equipment for continuation in these fields. These worries have been lessened by the excitement of some applications ranging from investigations of gas/liquid inclusions in rocks and minerals, to the quite spectacular radiographs of uranium distribution in kidney sections, using solid state track devices.

Although our interests lie primarily with an understanding of the polluting processes in uranium mine tailings, it has become obvious that the problem is a general and widespread one. Few physics investigations have been recorded and yet diffusion processes appear to be of prime importance. Most, if not all, the pollution arises from heavy metals other than uranium.

Interest in reactor safety has moved steadily away from the neutronics to the study of the hydrodynamics of the loss of coolant accident and to an understanding of the convection processes in transient heat transfer. Interesting problems in classical physics have arisen.

The main code development interest has been with a new method of numerical iteration which offers prospects for reducing the convergence time of large, three-dimensional codes. Work on interactive computing methods has considerably improved the efficiency and flexibility of the Division's computer operations and many interesting ideas have arisen, some of which are being pursued vigorously.

Most of the reactor physics work in the period has been involved with service type work on thorium in the fuel cycle, safeguards and preliminary work on a new research reactor.

2. REACTOR STUDIES

2.1 Moata Operations (T. Wall)

Moata was operated for a total of 33 MWh in the year ending August 1977, bringing the total fuel burnup to 211 MWh. Uranium assay and neutron radiography were the principal uses among a wide variety of service applications.

A comprehensive revision of all Moata documentation is expected to be completed early in 1978.

Uranium Analysis

Demand for the uranium analysis service from outside organisations increased in 1977. Of the 5400 total samples analysed to date this year, 3000 were for non-government bodies, 960 for the AAEC Exploration Division and the remainder for other AAEC customers. Since a commercial service was offered in June 1974, 24 545 samples have been analysed. Another uranium analysis rig (X193) has been built and installed at HIFAR, and is expected to be operationally available by the end of the year.

Neutron Radiography

(T. Wall, P. Gillespie*, S. T. Willatt[†])

Routine radiography of Qantas door thrusters continued on a basis of approximately two per month.

The development of root growth in certain plants is under study using the Moata neutron radiography facilities. Neutron radiography gives photographic contrast between roots and soil under natural growing conditions, which cannot be obtained with X-ray or other techniques. Time sequence neutron radiographs have been produced clearly showing the rapid growth of root systems (Figure 2.1)

Distribution of Uranium in Animal Tissue

(T. Wall, K. Bently^{††})

Solid state fission track recorders (SSTRs) are being used to study uranium distribution in biological tissues. Sections of tissue from mice kidneys in contact with mica SSTRs were irradiated in Moata and a clear fission track distribution corresponding to the uranium distributions in the sections was produced after etching the SSTRs. This enables areas of known tissue damage to be correlated with high uranium concentration.

Uranium in Fertilisers

In a joint project with the New Zealand Department of Scientific and Industrial Research and the Rothamstead Experimental Soils Research Station, United Kingdom, the fate of uranium deposited as superphosphate on test plots of fertilised soils has been determined. Samples of soils from 'control' and fertilised plots at Rothamstead taken in several years since 1870, have been analysed using delayed neutron activation analysis technique. The high precision of this method enabled the conclusion to be reached that nearly all the uranium contained in the superphosphate remains in the soil over the long period that phosphate fertilisers have been used at Rothamstead.

*Materials Division, AAEC

[†] La Trobe University, Bundoora, Vic.

^{††} Occupational Health Research Section, AAEC

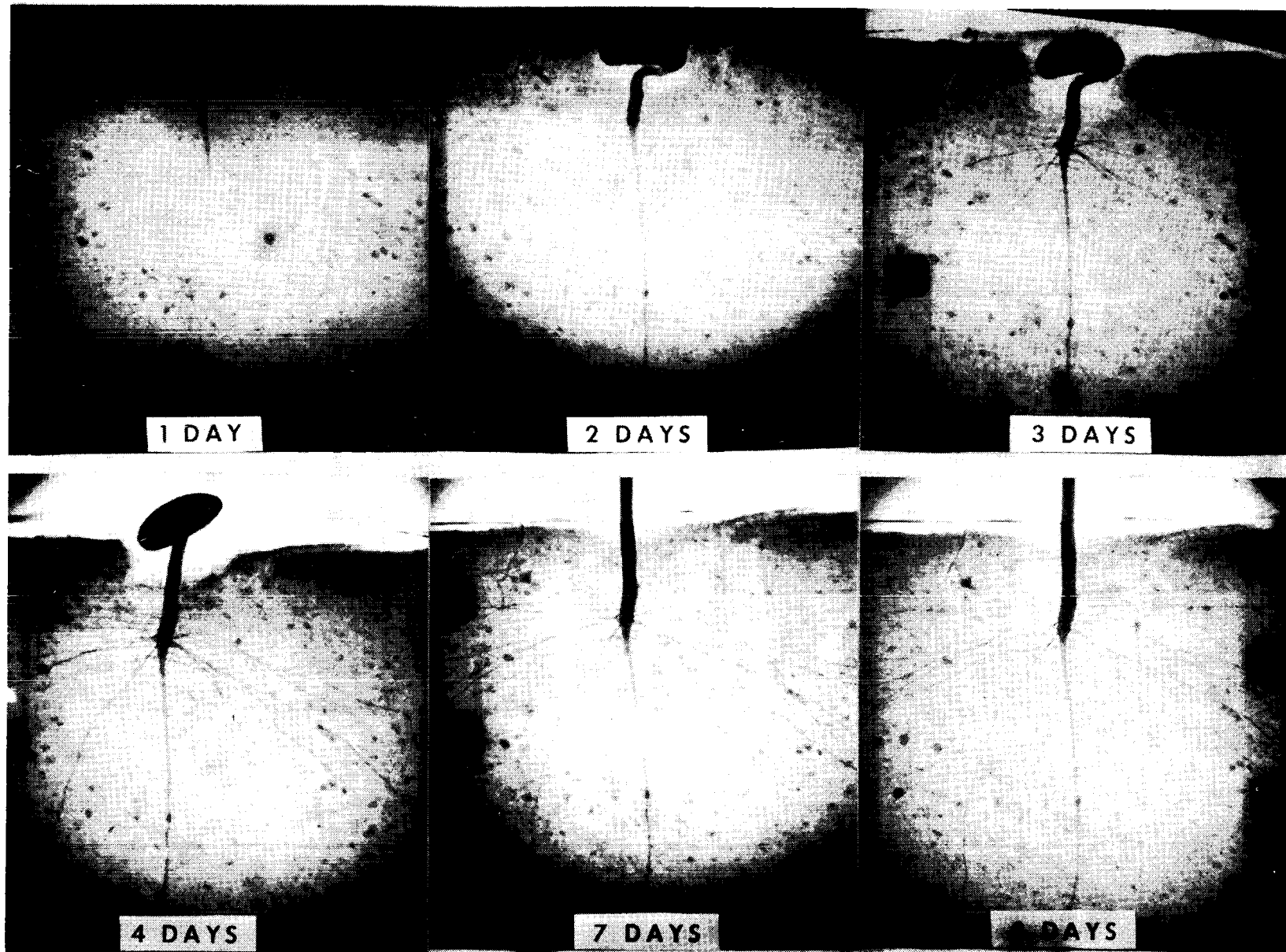


Figure 2.1 Development of bean seed root system: time lapsed neutron radiography

2.2 Reactor Physics Experiments

2.2.1 Critical Facility (D. B. McCulloch, G. Durance)

Analysis of the FCl 'hard-spectrum' core experiment was completed. Generally good agreement with AUS/ENDF/B-IV calculations was obtained for most measured parameters. A large unresolved discrepancy remains between measured and calculated values of the 'central' reactivity worth of a perturbing ^{235}U sample. This is believed to be due to difficulties in simulating the cell so as to calculate a reliable fine structure flux correction between the actual perturbation position and the 'cell average' condition to which the perturbation calculation applies. An empirical modelling situation was reached and further effort to reduce the discrepancy was not considered justified.

Further experimental work awaits clarification of the direction of the Commission's fission reactor program.

2.3 Integral Pulsed Neutron Experiments with Heavy Metal Assemblies

(M. Rainbow, I. Ritchie)

(a) Thorium Assembly

Measurements of the time-dependent ^{235}U reaction rate in the thorium assembly with a pulsed $\text{Li}(p,n)$ source have been repeated. The decay rate of the fundamental Fourier spatial mode was again found to vary quite markedly with time, but not in the same manner as previously observed. A thorough investigation did not support the suspicion that the quite complex method of data analysis (see below) might have been responsible for the effect.

Because of the difficulties experienced in the analysis of the measurements, a new approach was adopted. Previously, time-dependent detector reaction rates, measured at a large number (usually 39) of spatial locations, were Fourier analysed to give the time-dependent detector reaction rates associated with the various Fourier spatial modes. The time-dependent detector reaction rate associated with the fundamental Fourier spatial mode was then compared with the time-dependent detector reaction rate as calculated by the zero-dimensional diffusion theory code TENDS, which uses a DB^2 term to describe leakage.

In the new approach, the time-dependent detector reaction rates are measured at some specific location within the assembly. These are then compared directly with the results of a calculation performed with the multigroup Monte Carlo transport code MORSE, which can handle time-dependent problems in complex geometry. The input, output and data accumulation subroutines of the code have been modified to suit the peculiarities of the pulsed neutron problem and to improve accuracy. To facilitate the efficient use of the results the MORSE calculations are done with a source having a narrow (short duration) rectangular form. Calculated time-dependent detector reaction rates for comparison with experiment are synthesised by convoluting the code output with a histogram representation of the experimental source pulse profile. As a result, if a particular experiment is repeated and a different source pulse profile pertains, a new MORSE calculation is not required.

(b) Depleted Uranium Assembly

Measurements have been made of ^{235}U and ^{237}Np time-dependent reaction rates in the depleted uranium assembly using a pulsed $\text{Be}(d,n)$ source. The results are presently being analysed and compared with the results of MORSE calculations using the ENDF/B-IV data file. Figure 2.2 shows a comparison of a measured versus a calculated time-dependent ^{235}U reaction rate. The curves have been normalised at 150 ns. Figure 2.3 shows a comparison of the 'instantaneous decay rates' of the experimental versus the calculated curve as a function of time. These results show that at late times there is reasonable agreement between theory and experiment, but at early times,

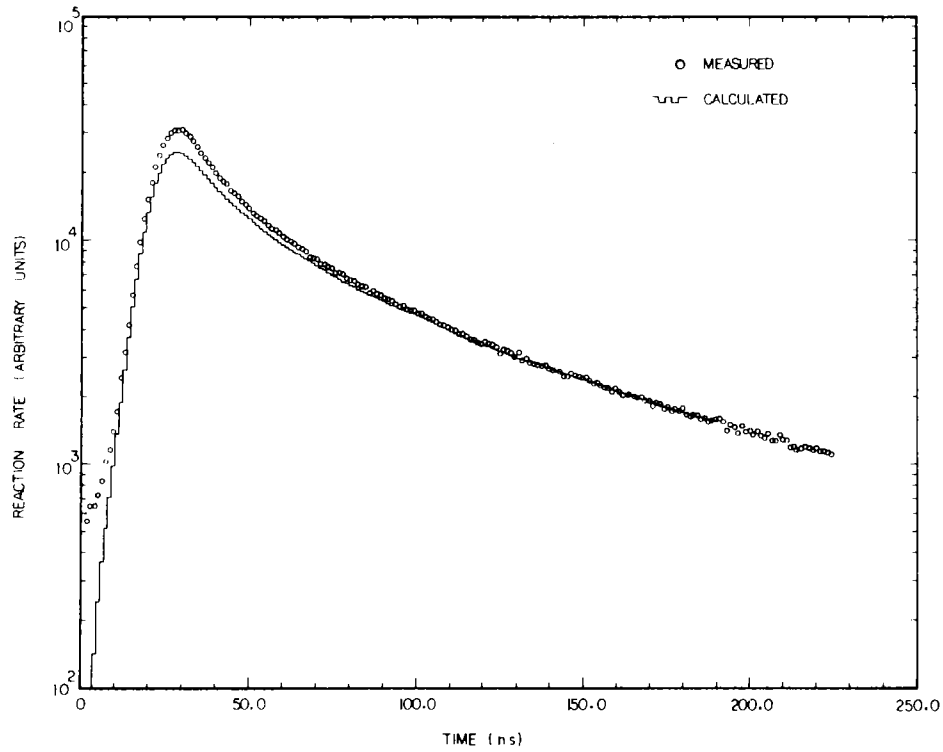


Figure 2.2 Time dependent ^{235}U reaction rates in depleted U assemblies

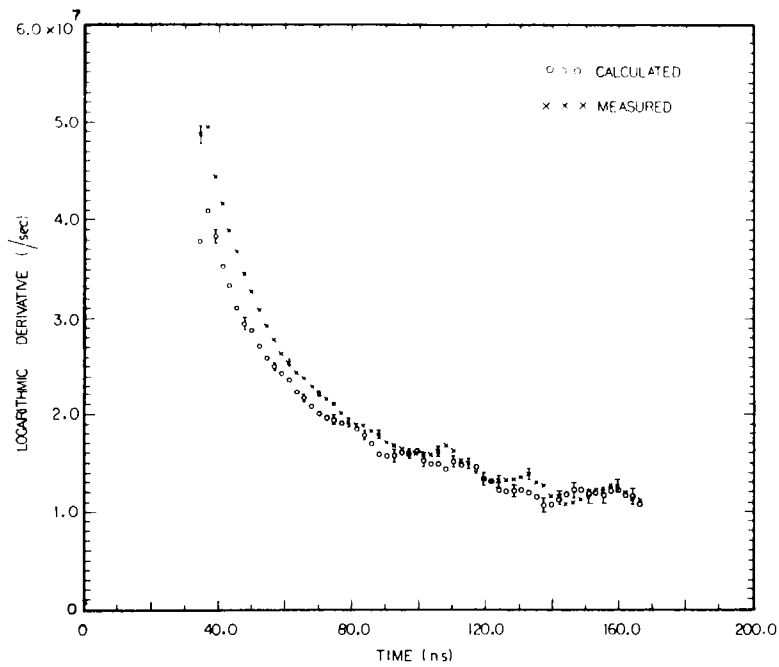


Figure 2.3 Instantaneous ^{235}U reaction decay rate in depleted U assemblies

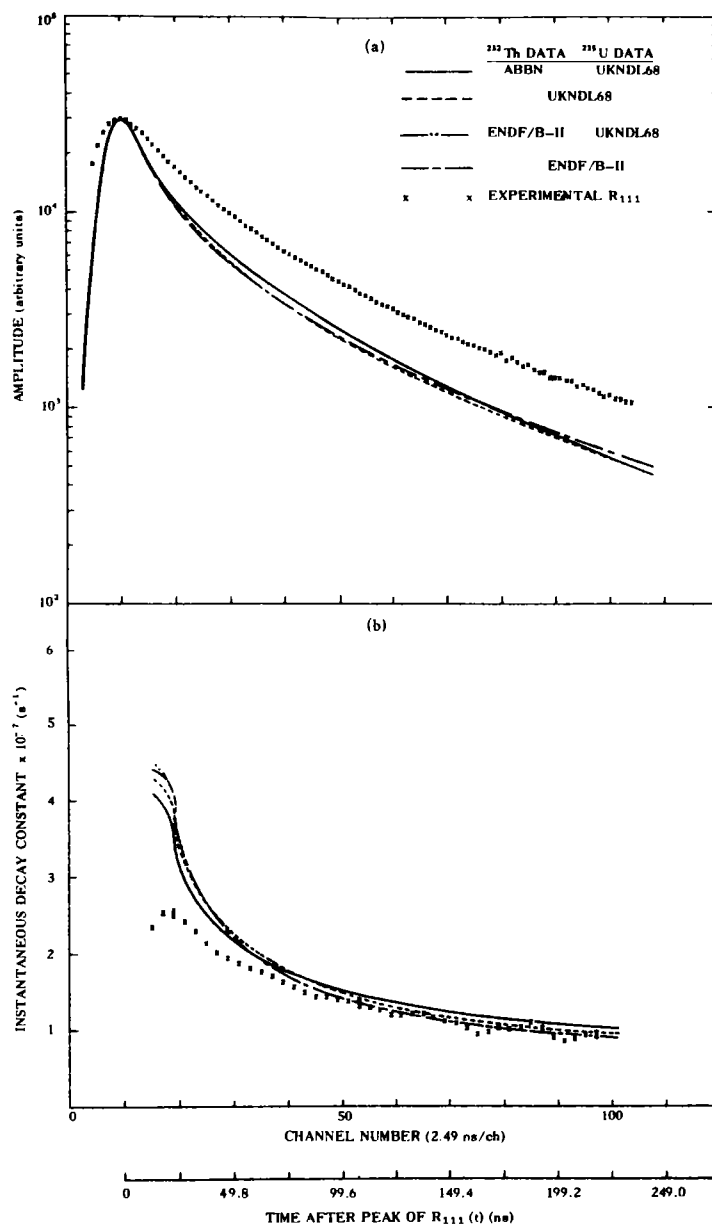


Figure 2.4 Fundamental mode reaction rates,
measured and calculated

the calculated decay rates are much slower than the experimental ones.

It is interesting to compare these results with earlier results (Figure 2.4) obtained for the time-dependent ^{235}U reaction rate in the thorium assembly with a pulsed Be(d,n) source. The results for the thorium assembly also exhibit reasonable agreement between experiment and calculation at late times and marked disagreement at early times. However, in contrast to the results for the depleted uranium assembly, the results for the thorium assembly show that the calculated reaction rate decays too fast.

The two sets of calculations and experimental results are not quite comparable in that the uranium assembly reaction rates are measured and calculated at discrete points, while the thorium assembly results are for the lowest Fourier mode. However, since calculations for the depleted uranium assembly decays slower than experiment at all points (7 in all) considered and since, with the source at the centre, the fundamental mode is the dominant mode at all points, it is likely that the difference in the results for depleted uranium and thorium is significant.

2.4 Time-Dependent Spectra in Heavy Metal Assemblies (S. Whittlestone, I. Ritchie)

Development of small ($\sim 0.5 \text{ cm}^3$) detectors filled with the liquid scintillator NE213 has continued. Their good ($\sim 1 \text{ ns}$) timing resolution will be of significant advantage in measuring time-dependent spectra in heavy metal assemblies. A second, small quartz scintillator chamber delivering $\sim 26\%$ more light output has been manufactured and tested.

The detection efficiency of the scintillation detectors was determined using the associated particle rig at the Australian National University, where the combination of a cyclotron and a tandem Van de Graaff accelerator produced neutrons with energies in the range 2.5 to 14 MeV. As well as providing a valuable experimental calibration of the detectors, these experiments demonstrated that the light output from recoil carbon nuclei is less than values currently accepted.

A number of measurements have been made to ascertain the significance of various sources of systematic error in time-dependent spectra measurements. Perturbation of the neutron energy spectrum in the assembly by the hole in which the detector is placed and by the detector itself has been shown to be negligibly small. Amplifier gain drifts have been measured and shown to be acceptable provided the system is given some six hours to settle down after switching on the photomultiplier high voltage.

Other sources of error investigated were timing drifts and walk. Small ($\sim 2 \text{ ns}$) drifts due to changes in the accelerator beam pulse shape or time to amplitude converter (TAC) shifts can be tolerated because a second scintillator has been set up to monitor the beam pulse. Its output is gated in such a way that the time spectra from the monitor and the detector are processed by the same TAC and stored in the same time spectrum on the pulse height analyser. Drifts only broaden the time spectrum and can be allowed for using information from the monitor time spectrum.

The more serious timing problem is walk - the systematic shift in timing according to the amplitude of the detector pulses. With the rapidly varying count rates encountered, a walk of only 1 ns can cause severe distortion of time-dependent pulse height spectra. Since the most meticulous adjustment of the constant fraction timing system did not reduce the walk below 0.6 ns for a 40:1 dynamic range, a data processing program was developed for the on-line computer used to collect the time-dependent pulse height spectra which shifts the storage channel of each event in the time spectrum according to its pulse height, by an amount based on previously measured walk versus pulse height curves. The on-line program works well. The overall accuracy of the correction technique is currently being tested.

It is anticipated that the detector system will allow measurement to be made of time-

dependent neutron energy spectra in pulsed heavy metal assemblies over the range 0.5 to 5 MeV with a timing resolution of <1 ns.

2.5 Neutron Spectrometry

2.5.1 Neutron energy spectra from thick target Li(p,n)Be sources (A. Rose)

The measurement of the angular distribution of neutrons from the Li(p,n)Be reaction has been completed. Neutron spectra were measured at angles of 0, 30, 60, 90 and 120 degrees over the neutron energy range 0.08 to 0.9 MeV.

Comparison between these measurements and calculations are in agreement within the errors which are 5% for measurements and 10% for calculation.

Yield measurements by others using thin lithium targets and data obtained by measuring yields at particular energy points are compared in Figure 2.5 with the 0° thick target measurements made here. In general, the agreement is good, although at low energies (0.2 MeV) the present measurements are on the high side, but nevertheless, within the errors. A comparison of the parameter peak (0.56 MeV) to valley (0.31 MeV) for the various experiments indicates that the present measurements gave a low value. It is possible that neutrons scattered from the target vicinity arrive at the detector with energies corresponding to the valley energy. However, calculations show that this effect is small (about 1%).

2.6 Reactor Safety

2.6.1 LOCA analysis (W. J. Turner, A. W. Dalton, G. M. Trimble)

Australian participation in the OECD-NEA/CSNI Working party on Emergency Core Cooling continues and further work has been done with NAIAD on the Standard Problems.

For Problem 3, agreement between our NAIAD calculation and the experimental data was as good as, or better than, that for any other solution submitted. This is illustrated in Figure 2.6 for the mass of fluid remaining in the blowdown rig. The Swedish RELAP 4 calculation shown in this figure represented the closest agreement with experiment for all RELAP 4 results submitted, the others being from the USA, Switzerland and Euratom.

Problem 4 (Semiscale Blowdown S-02-6) was the first attempt to use NAIAD for a PWR blowdown situation and is the most complex problem attempted to date. In contrast with Problem 3, all Problem 4 calculations were completed and submitted before the experimental results were released. Agreement between NAIAD and experiment was better than some and worse than other calculations submitted (Figure 2.7).

Standard Problem 6 (blowdown of a large pressure vessel through a small pipe at two-thirds height) has been studied and preliminary calculations completed. The results suggest that non-equilibrium effects, which the present version of NAIAD cannot allow for, may be important.

NAIAD modelling of the Engineering Research Division's blowdown experiments continued. Refinements to allow for heat transfer from the pressure vessel to the fluid during the transient and for the flow restriction due to the heater, did not significantly improve the measure of agreement between experiment and calculation reported in AAEC/PR42-P.

More detailed investigation of exact transient histories showed that the experimental discharges occurred in two distinct stages. This resulted from retention of a definite boundary between two fluid states, one of high and one of low quality. The calculation, however, rapidly passes to a single fluid whose quality varies smoothly over the length of the pressure vessel. It appears that countercurrent upward flow of bubbles in the vertical pipe sections is important and would have to be incorporated in the NAIAD model to allow realistic simulation of these experiments. In addition, the very large temperature gradients in the liquid between the pressure vessel and the test section caused choking to occur upstream of the pressure tapping.

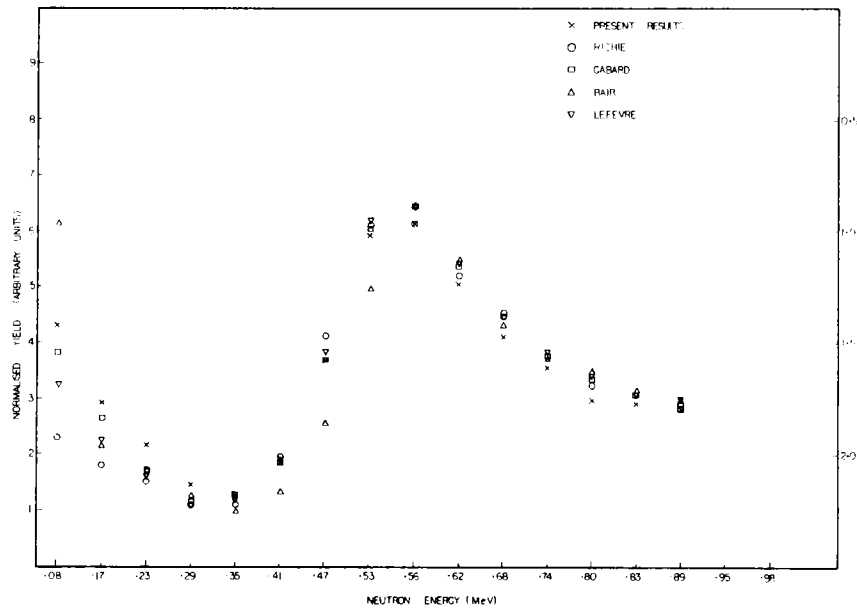


Figure 2.5 Neutron yield at 0° from $\text{Li}(p,n)$ reaction

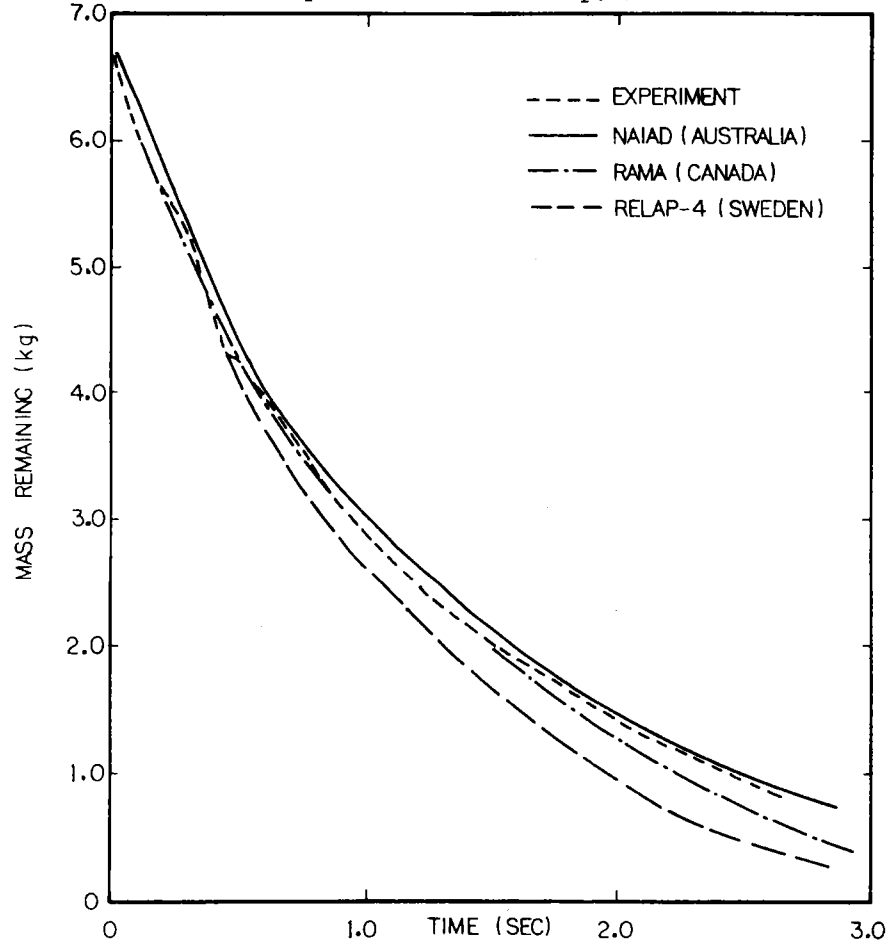


Figure 2.6 Mass of fluid in rig in first few seconds after blowdown

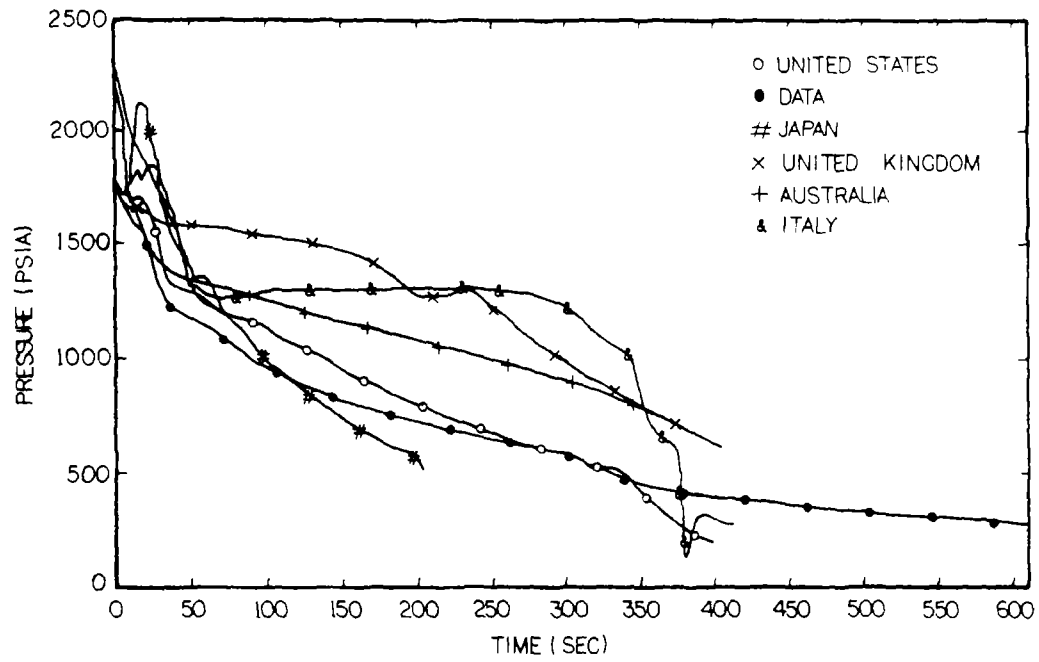


Figure 2.7 Time behaviour of blowdown pressure in semiscale experiment S-02-6

This (internal choking) effect cannot at present be represented in NAIAD. Overall, the studies have provided valuable pointers to features to be incorporated in further developments of the NAIAD scheme.

The NAIAD code has been supplied to the NEA Computer Program Library, Ispra, and to the Argonne Code Center Library, USA.

2.6.2 Reactor transient studies (J. W. Connolly)

Calculations were made of self-terminating power transients following hypothetical reactivity additions to HIFAR using the model developed for analysis of forced flow SPERT II transients (Connolly and Harrington 1977)¹. A revised version of the ZAPP code (Ferguson 1977)² allowing cylindrical geometry was required and in order to test this revision and provide more stringent checks of the forced flow model, a comprehensive comparison of calculation with experiment was made for the SPERT III-E core.

The SPERT III-E oxide core was a small mockup of a typical PWR core. Power transient data were obtained for a range of initial core conditions corresponding to those encountered in operating a commercial unit. A description of this reactor and the experimental results have been given by McCardell et al. (1962)³. The fuel pin consisted of a UO₂ pellet, radius 5.334 mm, a helium gas gap of 0.076 mm and stainless steel cladding, thickness 0.508 mm. These pins were mounted in the fuel elements in a 5 x 5 array on a square lattice pitch of 14.86 mm. The coolant area was converted into an annular region of the same area for the ZAPP cell representation. The value of the gas gap thermal conductivity was taken from data given by McCardell et al., as were values of the fuel Doppler coefficient and coolant void coefficient. The coolant spectrum reactivity coefficient was inferred from the data of McCardell et al. by assuming a reflector spectrum reactivity coefficient of $10^{-4} \delta k/k \text{ } ^\circ\text{C}^{-1}$ (Wajima and Yamamoto 1965⁴).

The system conditions for the E-core experiments were as follows:

<u>Accident Conditions</u>	<u>Coolant Inlet Temperature</u>	<u>Initial Reactor Power</u>
Cold startup	21 ^o C	5 x 10 ⁻⁵ MW
Hot startup	127 C or 260 C	5 x 10 ⁻⁵ MW
Hot standby	260 ^o C	1 MW
Operating power	260 ^o C	20 MW

ZAPP calculations of cold startup transients are shown in Figure 2.8. Excellent agreement with experiment is shown over the whole range.

A comparison of calculated and measured burst parameters for a representative range of hot startup excursions is given in Table 2.1. Good agreement between experiment and calculation is demonstrated.

¹Connolly, J. W. and Harrington, B. V. (1977) - An analysis of power transients observed in the SPERT II D₂O moderated close packed core. AAEC/E418.

²Ferguson, H. T. (1977) - AAEC unpublished work.

³McCardell, R. K., Herborn, D. I. and Houghtailing, J. E. (1962) - Reactivity accident test results and analyses for the SPERT III-E core - a small oxide fuelled, pressurised water reactor. IDO-17281

⁴Wajima, J. T. and Yamamoto, K. (1965) - Temperature coefficient of water lattices. J. Nucl. Sci. and Tech. 2, 9, 331-339.

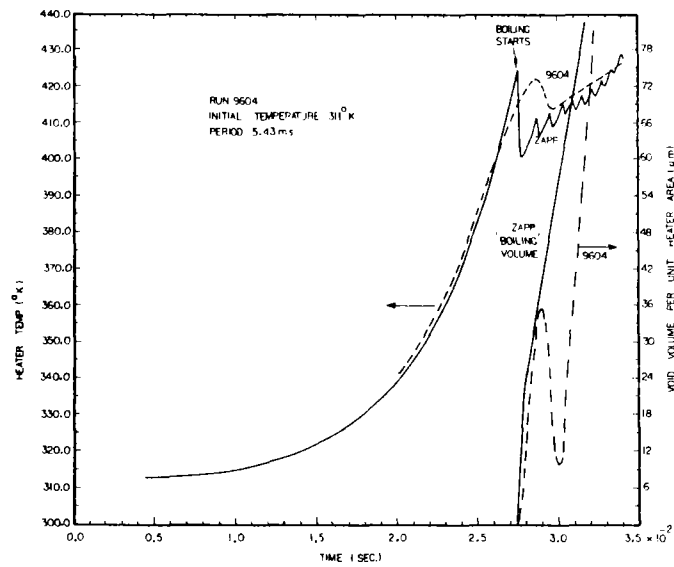


Figure 2.8 Peak power in SPERT III-E cold start up transients

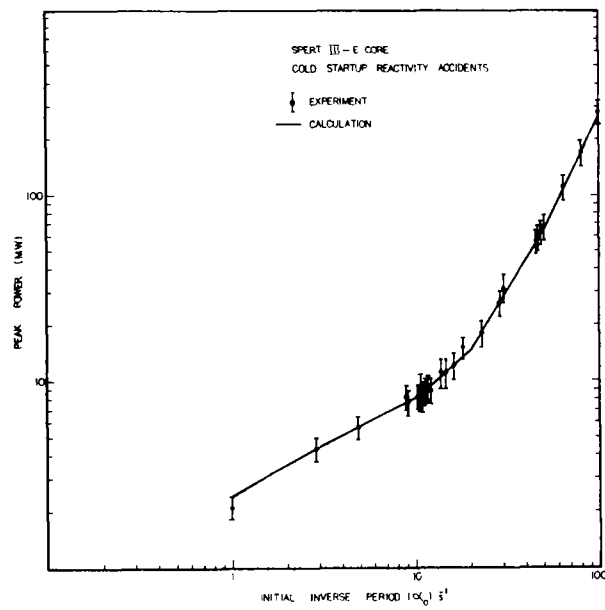


Figure 2.9 Modelling of water cooled heater temperature transients

TABLE 2.1
HOT STARTUP EXCURSIONS

α_o (s ⁻¹)	Flow (ms ⁻¹)	P _{max} C (MW)	P _{max} E (MW)	C/E	E _{tm} C (MJ)	E _{tm} E (MJ)	C/E
Initial Temperature 120°C: Pressure 10 MPa							
97.1	4.27	295	280±42	1.05±0.15	6.25	6.3±1.1	0.99±0.17
51.0	4.27	86.7	78±12	1.11±0.15	3.50	3.2±0.5	1.09±0.16
23.5	4.27	23.7	22±2	1.08±0.14	2.29	2.0±0.3	1.14±0.15
9.8	4.27	10.7	9.1±1.4	1.17±0.15	4.27	4.3±0.7	0.99±0.16
4.78	4.27	7.8	6.8±1.0	1.15±0.15	~9.5*	7.6±1.3	-
14.3	6.70	13.6	11±2	1.24±0.18	2.77	3.2±0.5	0.86±0.16
8.48	7.3	9.6	7.8±1.2	1.23±0.15	5.39	4.8±0.8	1.12±0.17
Initial Temperature 260°C: Pressure 10 MPa							
103	4.27	475	410±41	1.16±0.10	9.13	8.5±1.1	1.07±0.13
48.5	4.27	115	97±10	1.18±0.11	4.77	4.5±0.6	1.06±0.13
14.24	4.27	19.8	16±1	1.24±0.12	4.44*	3.3±0.4	-

*Broad topped bursts - E_{tm} not well defined

Only a limited number of hot standby and operating power transients were measured in the experimental program, and all tests were for a coolant flow rate of 4.27 ms⁻¹. Table 2.2 shows the results of experiment and calculation. In the case of operating power transients, it was found that the calculations were very sensitive to the rate at which the excess reactivity was inserted. This is because the initial power level was so high that reactivity feedback commenced while the reactivity was being inserted and the reactor never attained an asymptotic period. The rate of reactivity insertion was estimated from rod withdrawal rates given by McCardell et al. (1962) as 0.121 s⁻¹; the effect of increasing this to 0.125 s⁻¹ is also given in Table 2.2.

TABLE 2.2
HOT STANDBY AND OPERATING POWER EXCURSIONS

Reactivity Insertion (δk/k)		P _{max} C (MW)	P _{max} E (MW)	C/E	E _{tm} E (MW)	E _{tm} (MW)	C/E
0.00959	Hot	141	120±10	1.18±0.08	4.9	4.5±0.6	1.09±0.13
0.0108	Standby	704	620±60	1.13±0.10	11.3	11±1	1.03±0.09
0.121 s ⁻¹	Operating	439	610±60	0.72±0.10	11	17±2	0.64±0.12
0.125 s ⁻¹	Operating	590	610±60	0.97±0.10	13	17±2	0.76±0.12

Again, satisfactory agreement between experiment and calculation is obtained, although the operating power test would require very precise knowledge of reactivity insertion rates to make the comparison meaningful. Examination of the reactivity compensation data shows that the major part comes from the Doppler effect in the fuel and this fact, together with the low thermal conductivity of the oxide fuel, makes these transients relatively insensitive to flow rate compared with the highly enriched, thin fuel plates of the SPERT II reactor.

2.6.3 Transient boiling heat transfer (J. W. Connolly)

The general success of the boiling heat transfer model used in ZAPP has led to an attempt to elucidate the physical phenomena suggested by the model. To this end the experiments reported by Johnson et al. (1961)* have been analysed and a review of existing theories of the development of nucleate boiling undertaken.

The Johnson experiments involved the exponential heating of very thin (0.02-0.2 mm) metal ribbons immersed in water, and are thus free of the complications involved in a reactor transient situation. In particular, the low thermal capacity of the ribbon means that when nucleate boiling commences, the increase in heat flux leads to a drop in ribbon temperature, providing a reasonably sensitive indicator of the temperature at which boiling commences. The magnitude of this temperature drop also provides a means of assessing the initial thickness of the water layer undergoing nucleate boiling.

It was found possible to reproduce a wide range of temperature data from these experiments using the ZAPP code if a superheat of 20°C was assumed to be necessary to initiate nucleate boiling and the initial boiling layer adjacent to the heater surface was 0.02 mm thick. Further, the rate at which the 'boiling' volume developed in the ZAPP calculations bore a close similarity to the bubble void growth rate determined by experiment, although without the initial void collapse following the heater temperature set-back. These results are illustrated in Figure 2.9 for a 5.4 ms period energy input to a 0.025 mm platinum ribbon.

Work is continuing towards an understanding of void volume development under conditions of rapidly increasing heater surface temperature, as this provides the major shutdown mechanism for severe transients in water moderated reactors.

2.7 HIFAR

2.7.1 Reactor dynamics (J. R. Harries, D. J. Wilson)

An understanding of the dynamic behaviour of HIFAR power is necessary for a full reactor safety evaluation. The previous experimental data on the dynamic behaviour obtained by slowly changing the D₂O temperature has been supplemented by observing the power transients produced by changing the number of primary coolant circulation pumps.

Switching on the third D₂O circulation pump causes the D₂O flow to increase from 400 to 475 kg s⁻¹ in a few seconds. The immediate effect of this change in flow is to reduce the temperature rise in the fuel elements, producing a sharp but small increase in power. After a few seconds, the D₂O, which has now been less cooled in passing through the heat exchangers, begins to enter the fuel elements and causes a decrease in the reactor power. About 10 seconds after the transient starts, cooler D₂O from the RAT has time to circulate around the primary circuit and the power again rises. Eventually the temperature rise of all the D₂O in the primary circuit causes the power to stabilise.

The sequence of events in the flow transients is complex and could only adequately be analysed to developing a dynamic model of HIFAR. The primary coolant circuit was divided into five functional components: the heat exchanger, the risers, the fuel elements, the reactor aluminium tank and the downcomers. The heat exchanger characteristics were calculated as a function of the inlet temperature and flow rate for both the D₂O and the H₂O. The risers and the downcomers were present mainly as delays with some mixing due to the turbulence and velocity profiles across the pipes. The heat added in the fuel elements is a function of the reactor power and the D₂O flow rate. The heating effect of the circulation pumps and the thermal

*Johnson et al. (1961) - Temperature variation, heat transfer and void volume development in the development in the transient atmospheric boiling of water. SAN-1001

capacity of the pipework is also included.

The model of the primary circuit was interfaced to a neutron kinetics calculation in the HIDYN code. The reactivity used in the neutron kinetics depends on the temperature of the D₂O entering the core, the D₂O flow rate and the power level, while neutron kinetics calculations in turn determine the power level and hence the heat added to the D₂O. The calculated power profiles corresponding to the measured temperature and flow transients showed reasonable agreement. Figure 2.10 compares the measured data with HIDYN power profiles calculated for two different values of the temperature coefficient of reactivity, α .

2.8 Deep Ocean Currents and the Disposal of Radioactive Waste into the Ocean

(J. R. Harries)

The evaluation of proposals by several countries to deposit radioactive waste into the deep ocean is made difficult by the general lack of knowledge about deep ocean circulation. Experimental measurements of the currents near the ocean floor are expensive in time and money and the theoretical treatment is limited by the capacity of computers to model topography and mixing phenomena on a small enough scale. Nevertheless, the present somewhat inadequate understanding of deep currents must be used to set accepted international limits on the disposal of radioactive waste. The lack of knowledge has forced the international committees that define the limits to use vastly simplified ocean models.

A study is being undertaken to investigate the effect of the international limits on the local Australian situation. Australia has coastal regions in both the Indian and Pacific Oceans and hence it is important for us to estimate the likely consequences if disposal should occur in either ocean.

The conditions in the deep oceans in the vicinity of Australia are being studied to identify local problems before ocean disposal becomes more widespread. Most of the problems are not unique to radioactive waste, but are common to any material added to the ocean, whether intentionally by disposal operations, or unintentionally via rivers. The deep ocean circulation patterns are being estimated from the published data and the mean flow identified. There are, however, considerable uncertainties about the variability and timescale of the flow. The distribution of naturally occurring radioactive and stable tracers in the ocean shows that the transport of ocean pollution depends strongly on both the elements and the chemical species present. Some elements associate with sinking particulate matter, which provides rapid transport from the surface to the ocean depths. These elements might be incorporated into the sediments or, alternatively, they might redissolve under the conditions present at great depths.

2.9 Applications

2.9.1 Thorium analysis by neutron activation and gamma spectrometry

(G. Durance, D. B. McCulloch)

Neutron capture in ^{232}Th leads to the production of ^{233}Pa , whose β -decay with 27.0 day half-life to ^{233}U is accompanied by emission of a γ -ray of energy 311.8 keV. It appears that by suitable choice of irradiation and cooling times, this γ -ray can be rendered relatively free from interference by other γ -rays emitted from typical activated geochemical samples, including those containing significant uranium. A thorium analysis technique based on this process could offer substantial advantages over such alternatives as delayed neutron activation or proton induced X-ray emission.

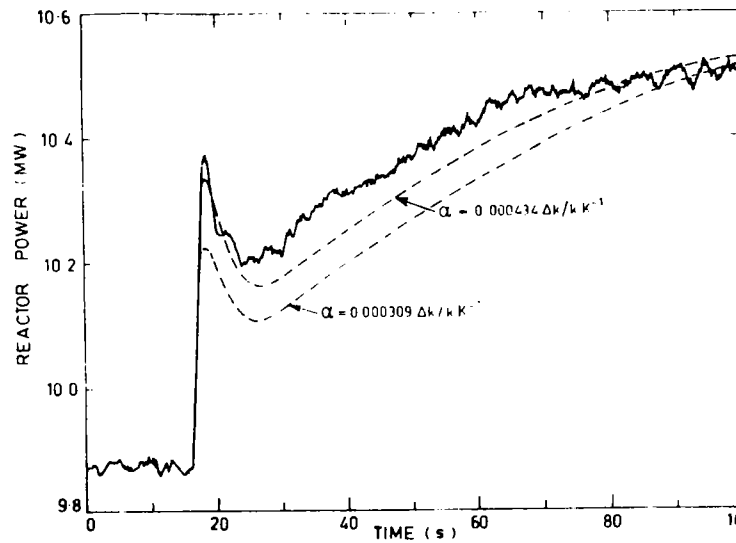


Figure 2.10 Hifar power transient resulting from increased coolant flow

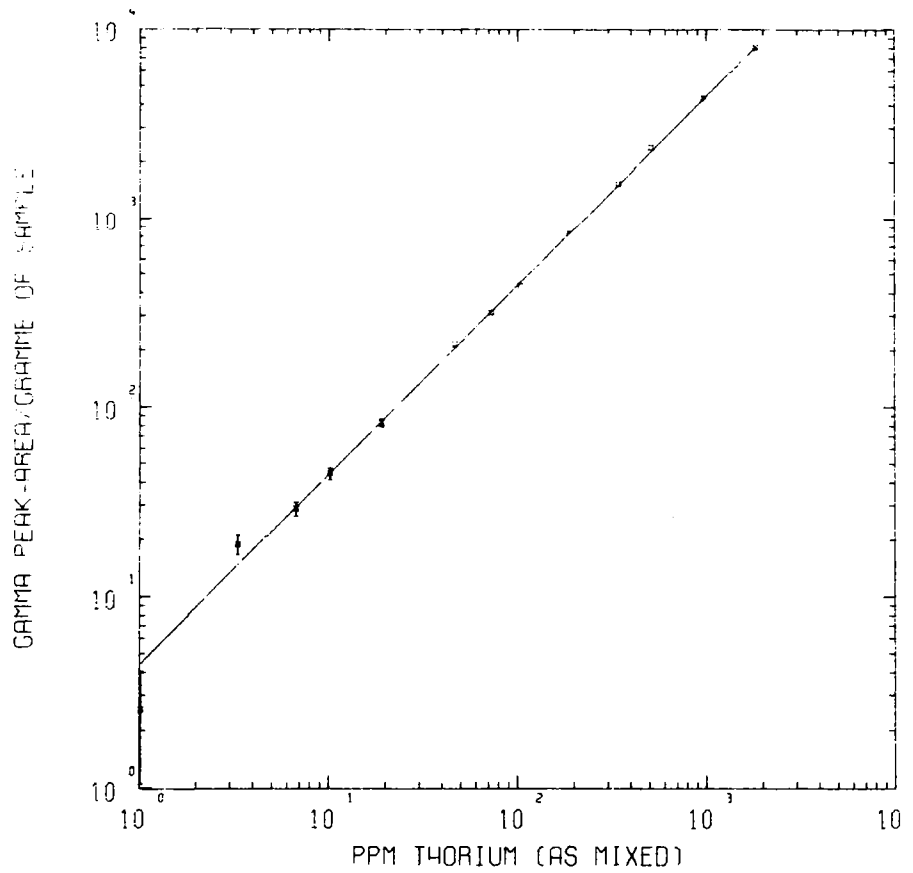


Figure 2.11 Gamma activity from thorium ore samples as function of thorium concentration

Preliminary experiments to investigate the potential of the method for routine quantitative assay of thorium in mineral ore samples appear promising. Crushed thorium bearing samples of ~10 g total mass sealed in polythene capsules were irradiated in a flux of $\sim 10^{12} \text{ cm}^{-2} \text{ s}^{-1}$ for 5 minutes and the decay followed (after a suitable time interval) using a Ge(Li) detector in conjunction with a 4K ADC and PDO-7 computer.

Potential interference with the required γ -ray for a range of typical materials appears to arise primarily from any rare earths and uranium content. The latter, which gives rise to a 315.7 keV γ -ray from ^{239}Np , is generally more persistent, but even so can be reduced to negligible proportions for U:Th ratios up to ~8:1, provided a delay of ~2 weeks is allowed between irradiation and the start of γ -counting.

Samples made up from specially prepared $\text{ThO}_2/\text{CaCO}_3$ mixtures with thorium content ranging from 1 to 2000 ppm were irradiated and counted under the conditions as established above. The results (Figure 2.11) suggest that in this range, an accuracy of about 3% may be possible down to ~15 ppm, deteriorating rapidly down to a detection threshold of ~5 ppm

2.9.2 Neutron moisture meter investigations

(D. B. McCulloch, D. J. Wilson, J. A. Daniel)

Neutron moisture meters (IAEA, Vienna, 1970^{*}) have been widely used for many years in varied disciplines for in situ determinations of free water content in soil strata. Although the principles are simple, interpretation of field measurements requires neutron transport calculations to link observed count-rates to those obtained under known conditions in laboratory calibration experiments. This process has not generally been fully satisfactory, with the result that derived moisture content data have often not been as reliable as might be expected. A further consequence is that much effort has been expended in many working groups on laboratory experiments to derive empirical adjustments to calibration factors to suit particular experimental projects.

During a development of a neutron perturbation technique to measure the absorption cross section of soils containing bound hydrogen (McCulloch and Wall 1977[†]) it appears to us that much of the problem of interpretation of neutron moisture meter data might be attributable (i) to the use of very simplified neutron diffusion theory calculations which do not take adequate account of the finite size and geometrical details of the calibration experiments compared with field conditions, and (ii) to neglect of possible effects on neutron count rates of reflections from materials outside the calibration experiment drums.

Since there was a requirement for soil moisture determinations in connection with Rum Jungle environmental studies, and a general solution to the problem would be of widespread interest and benefit, development of a suitable calculational model and a small series of carefully controlled calibration experiments were begun.

Preliminary survey calculations quickly showed that the 'infinite geometry' generally assumed for the drums usually used in laboratory experiments was valid only for high soil water contents, well beyond the normal practical range. This alone appears sufficient reason for many of the interpretative difficulties which have persisted in the commonly used schemes. In addition, preliminary experimental data from a calibration drum filled with sand/polyethylene bead mixtures which neutronically simulates wet soil, while avoiding the problem of varying water content with depth below the surface, have (i) confirmed that neutron count rates in the drum are

^{*}IAEA, Vienna (1970) - Neutron moisture gauges. Technical Report Series No. 112

[†]McCulloch, D. B. and Wall, T. (1976) - Nucl. Instr. & Methods 137, 577-581

indeed very sensitive to surroundings in the laboratory, and (ii) show that two-dimensional neutronics calculations with careful attention to representation of the precise features of the experimental geometry are necessary if good agreement with measurements is to be obtained.

2.9.3 Pressure dependence of plasma formation under laser radiation (A. Rose)

A line selectable CO₂ laser has been used to measure breakdown thresholds in the UF₆ analogue gases (CF₃)C₆F₁₁ and C₆F₁₄ over the pressure range 0 to 100 torr. The maximum output power of the laser was 1.75 J with ~200 ns wide pulses at a repetition rate of ~1 pps and the power was varied by passing the laser beam through a variable pressure propylene gas attenuator.

The pressure at which breakdown occurred was found to decrease with pressure in a similar way for both gases. When all the results obtained were normalised to the same curve, the curve had a power law dependence on pressure with an exponent of $-2/3$ (Figure 2.12).

2.10 Neutron Source Project (G. Hogg, J. Tendys)

Investigations have been made on the time of emission of the neutron and X-ray pulses from the compressed plasma with respect to the state of compression of the plasma (as indicated by the time derivative of the current pulse). Neutron emission commences some 20 ns before the peak of the plasma compression and continues for 50-100 ns. Soft (<50 keV) X-ray emission also occurs at a similar time, but hard (>100 keV) X-ray pulses have been observed to commence 40-50 ns after peak compression. These measurements correlate with the general theory of the dense plasma focus.

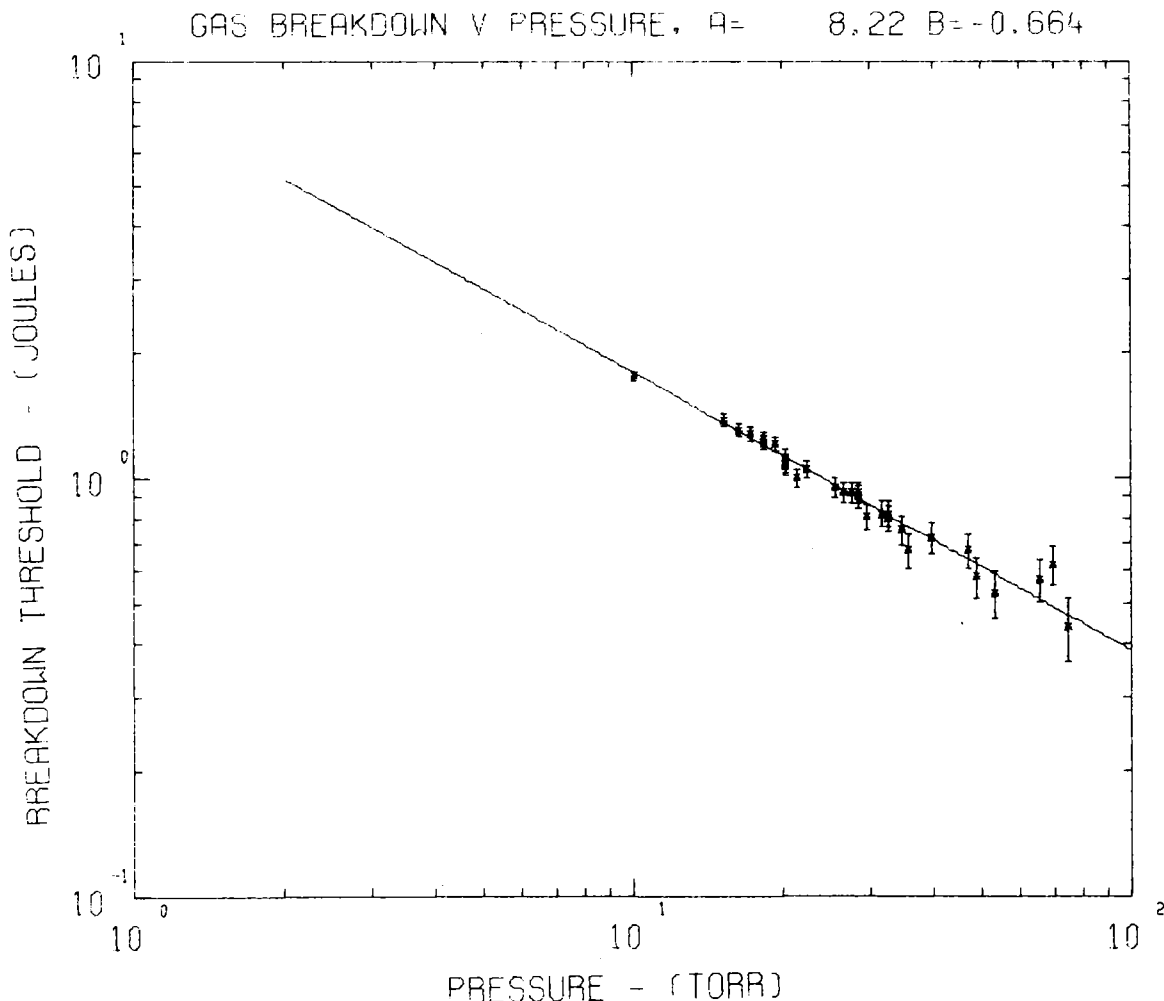


Figure 2.12 Plasma formation threshold as a function of gas pressure

3. NEUTRON PHYSICS

3.1 3 MeV Van de Graaff Accelerator: Operations and Facilities

(A. van Heugten, H. Broe, J. Fallon, L. Russell)

The accelerator was used for 2630 hours during the year. Time allocation for each experimental program is shown in Table 3.1. A major overhaul of the accelerator much reduced the time available for experiments. Because of voltage instability both the accelerating tube and belt were changed; the former after a life of 22 000 hours and the latter after a life of 8900 hours. The complete overhaul included the rebuilding of the alternator bearing housing and shaft to regain original dimensions and replacement, for the first time, of other components such as control rods.

Additional maintenance was incurred because of R.F. pulsing faults, electrical breakdown along the external pulse light pipes, chiller overhaul and the installation of an external gas supply to the ion source. As a result, the total down-time was 3020 hours. Some maintenance was carried out during accelerator operation.

Alternator Bearing Housing and Shaft

After every 1000 hours of running time, both the alternator and drive motor bearings are removed, cleaned, regreased and re-installed. The bearing housing and shaft suffers some degree of wear as a result of this operation. The alternator uses FAG UL Duplex type bearings, designed so that when installed in pairs they provide a predetermined amount of preload that eliminates any axial play within the bearing. Shaft location is effected in the usual manner by fixing the bearing position at one end only. The nature of the bearings requires that both the shaft and housings are machined to very close tolerances (shaft diameter = $50 \text{ mm}^{+0.006 \text{ mm}}_{-0.001 \text{ mm}}$; housing diameter $1100 \text{ mm}^{+0.016 \text{ mm}}_{-0.006 \text{ mm}}$).

After approximately sixty bearing services, excessive wear in the shaft and top housing caused bearing rotation of the inner race and consequent seizure. The top bearing housing and cover plate was rebuilt. The use of a bronze housing in lieu of a brass one should provide for less wear from bearing services and consequently longer life. The journals of the alternator shaft were remetalled and reground to specifications and dynamic balancing of the finished alternator was then carried out to manufacturer's specifications. Total down-time for this operation was five weeks.

Also during the year, non-availability of the UL bearings forced the use of UA bearings; these required shimming to provide appropriate preload. Close tolerance measurements were taken and 0.003" shims were manufactured and fitted. These bearings worked successfully until UL bearings were obtained.

Chiller

The chiller system, used to cool the accelerator, required an overhaul after many years of trouble-free running. This meant considerable down-time of the accelerator as unchilled tower water could not adequately cool both the accelerator and the Moata reactor. Work carried out included the installation of a water flow regulator to maintain constant head temperature at the compressor and flushing and cleaning of the entire system.

R.F. Pulsing

For several months the nanosecond pulsing facility continually detuned itself during operation. The problem was found to be the changing characteristics of two fixed value capacitors in the output stage when subjected to changes of pressure or heat. These capacitors have a solid dielectric and are epoxy filled. The changes that occurred were typically 3-5 pF in a total of 240 pF. There have been many hours of successful operation since replacement.

TABLE 3.1
ACCELERATOR TIME ALLOCATION - JULY 1, 1976 TO JUNE 30, 1977

Category	Experiment Title	Personnel	Origin	Running Time (hours)
Neutron Data				
Fission	Californium-252	Culley	Expt. Reactor Physics	54
Capture	Resonance Spectra	Allen, Kenny	Neutron Physics	193
	Capture cross sections	Allen, de Laeter, Cohen	Neutron Phys./WAIT/AINSE	24
Neutron Transport	Pulsed integral - thorium	Rainbow	Expt. Reactor Physics	416
	Pulsed spectra - thorium	Whittlestone	Expt. Reactor Physics	383
	Spectra - fast assemblies	Rose	Expt. Reactor Physics	48
Applications	Developments - prompt analysis	Bird, Russell, Scott	Neutron Physics	322
	Thorium analysis	Duerden	Expt. Reactor Physics	269
	AINSE projects	Cohen, Kanard	AINSE	140
	Gas flow analysis	Allen, Broe	Neutron Physics	78
	Glass analysis	Russell, Scott, Owen	Neutron Physics/ACI	572
	Oxygen diffusion profiles	Russell, Kanard, Singh	Neutron Physics/AINSE/Flinders	131

Total operating time 2630
Maintenance and development 3022
Unused time 3108

External Source Gas

Many of the earlier problems of an external three gas system have been solved. The major problem is the functioning of the gas line where it is adjacent to the equipotential rings. This occurs at random positions along the line, although many occurrences have been at the mid support plate. A completely satisfactory system is still not available after six months' work.

Light Pipes

After many years trouble-free operation, several light pipes had to be replaced. Voltage breakdown had occurred along the surface of the Perspex rods and the P.V.C. tape used to provide light insulation. There seemed to be some correlation between these events and gas line failure (mentioned above), although not in all cases. Untaped rods have been tried, but even with highly polished surfaces there is too much external light scattered into the system (from tank sparks, etc.) At this stage a system is proposed using filters to eliminate any light other than that produced by the pulsed light source; this system will eliminate P.V.C. wrapping.

Analysing Magnet, Flux Measuring and Control Systems

The nuclear magnetic resonance unit is required to measure field strengths in the analysing magnet with good resolution and accuracy. It has become unreliable during recent years, in spite of several modifications and repairs and has been replaced by a gauss meter/controller to provide highly stable magnetic fluxes (1 gauss in 4000 gauss). The gauss meter allows a required field to be selected using digit-switches and that field is controlled by feedback signals from a Hall effect probe, particularly when the magnet current is supplied by a solid state power supply. The magnet current is presently provided by a motor generator set. The fluctuations in output from this generator are short term in nature (<1 s). The new unit cannot follow these fluctuations and thus control the magnetic field adequately. The gauss meter/controller's long term stability as a measuring device has also been shown to be doubtful, with several gauss variations being typical over a period of, say, 8 hours.

Data Acquisition Facilities (M. D. Scott, R. J. Cawley)

The PDP-15 continued to serve as the principal data acquisition facility for accelerator experiments with surprisingly good reliability given the state of its I/O processor circuitry. Although there will be no further commitment to upgrade the PDP-15 main frame, development has continued on CAMAC standard data acquisition equipment which is transferable to other computers.

An ORTEC 800 ADC and associated CAMAC interface was installed. The data buffer incorporated in this interface provided a substantial reduction in deadtimes at high count rates and further improvements are expected with a larger data buffer memory.

The ORTEC 800 ADC and ORTEC 439 X-ray amplifier have been modified for signal compatibility and more rigorous accounting for deadtime due to pulse pileup.

Modifications have been incorporated into the PDP-15 supervisor system to avoid or survive hardware malfunctions in the I/O processor. As a result, it is no longer necessary for the user to turn off display before performing punch, read or Dataway operations.

Due to the improved reliability of PDP-15 I/O operations, the central computer disk store is routinely used for loading system and user programs into the PDP-15 and for storage and retrieval of data. The incidence of aborted experiments and frustrating delays due to PDP-15 unavailability has been much reduced. Consequently, unattended automatic sequences, experimental runs and increasingly sophisticated on-line analysis using FOCAL routines are practical.

In a typical run, one or more ADCs are used to collect pulse height spectra with continual fine adjustment of gain and zero as drifts are detected in spectrum peaks. Scalers count beam current integrator pulses ungated and gated by ADC-not-BUSY, pulser triggers also derived from current integrator pulses and 10 Hz clock pulses. At the completion of the run, signalled by overflow of one preset scaler, the scaler contents are used to calculate time of day, elapsed time, live time, average target current and the proportion of pulser events which found their way into the spectrum pulser peak.

If required, complete spectra are stored via Dataway or paper tape, then nominated positions are scanned for peaks and their precise positions, areas and continuum correction are printed, followed by corrected peak area renormalised to the accepted pulser events. Following this, or simultaneously, if data storage space permits, commands are sent to a stepping motor to move the next selected target into position, clear scalers and data space and commence a new run. Run duration and other parameters may be adaptively adjusted from one round of runs to the next.

A new version of the digital window dual parameter program has been developed. Based on the FOCAL 15 single parameter program, which has been successfully used with minor modifications for over a year, DIGWIN-F has extended the use of the FOCAL style language to all data acquisition tasks on the PDP-15. This has been accompanied by a steady increase in the appreciation and exploitation of the flexibility of the language by users. A version of DIGWIN-W is also available which corrects incoming counts for the monitor spectrum for 'walk'. The correction is applied on the basis of the pulse height of the coincident data count and is made before the window table is searched and the event stored.

PLOTS, a program which uses the PDP-15's small XY plotter to intercept items in the central computer PLOT queue, was written to provide labelled plots of data sent to the central computer via the Dataway.

The FOCAL language has also been incorporated in a new PDP-11 program CIZZAR. This program replaces the old PDP-7 program FISSER and allows flexibility in on-line data analysis and experimental control. The earlier PDP-11 multiparameter program has been modified to read the data sequencer programmer in a different order in a partially successful attempt to overcome data errors.

3.2 Fission Studies

3.2.1 Collaboration with Bruyères-le-Châtel (J. Boldeman, R. Walsh)

Boldeman and Walsh, under the sponsorship of the CEA, spent part of the year at the CEA laboratory, Centre d'Études de Bruyères-le-Châtel. They participated in measurements of the variation of the average total fission fragment kinetic and mass distributions in the neutron fission of ^{232}Th and gamma ray spectra following resonance neutron capture in ^{28}Si . A number of discrepancies between $\bar{\nu}$ measurements performed at Lucas Heights and at Bruyères-le-Châtel, particularly for the neutron fission of ^{235}U , were resolved.

3.2.2 Review of $\bar{\nu}$ values for thermal fission and ^{252}Cf (J. Boldeman)

A review of $\bar{\nu}$ values for thermal neutron induced fission and spontaneous fission of ^{252}Cf was presented at the International Specialist Meeting on Neutron Standards and Applications held at Gaithersburg, USA.

The paper concluded that following recent revision of the most accurate $\bar{\nu}$ measurements, there was no evidence to suggest that there exists a serious discrepancy between different methods of performing $\bar{\nu}$ measurements. The recommended values from this review are given in Table 3.2.

TABLE 3.2
RECOMMENDED $\bar{\nu}$ VALUES

Isotope	$\bar{\nu}_p$	$\bar{\nu}$
^{233}U	2.461 ± 0.008	2.468 ± 0.008
^{235}U	2.386 ± 0.007	2.402 ± 0.007
^{239}Pu	2.857 ± 0.010	2.863 ± 0.010
^{241}Pu	2.902 ± 0.010	2.918 ± 0.010
^{252}Cf	3.736 ± 0.010	3.745 ± 0.010

3.2.3 Revision of energy dependent $\bar{\nu}$ data for Pu isotopes

(J. Boldeman, J. Frehaut*, G. Mosinski*)

All $\bar{\nu}$ data for neutron fission of the plutonium isotopes have been revised. The most interesting feature to arise from this revision is the evidence that the $\bar{\nu}_p(E_n)$ data for ^{239}Pu exhibits some structure. In particular, there appears to be a hitherto unexpected minimum of approximately 1% near 100 keV neutron energy.

3.2.4 Measurement of the ^{252}Cf spontaneous fission neutron spectrum

(D. Culley, J. Boldeman)

The fission neutron spectrum from the spontaneous fission of ^{252}Cf has been accepted as the standard fission neutron spectrum. Despite this, the shape of the spectrum remains to be definitely established and there still exists a number of discrepancies in the data. The present measurement has been designed to provide an accurate determination of this spectrum with particular emphasis on the shape between 7-15 MeV.

The measurements involve the simultaneous recording of the neutron flight time over distances of 3-5 metres to the neutron detector and the energy response of the detector to provide a consistency check on the data. The neutron detector efficiency and its response have been determined for a large number of neutron energies between 2 and 10 MeV by the associated particle technique using the 12 MeV tandem accelerator at the Australian National University. The efficiencies have been determined with accuracies of approximately 2%.

Neutron time of flight data have been taken for three separate independent measurements and the analysis of the data is well advanced. The overall timing resolution for these experiments, including the effects of electronic drifts, etc., was approximately 2.4 ns for each of the three measurements. With a better ^{252}Cf spontaneous fission source and an improved fission detector, it is hoped to improve the overall timing resolution to approximately 1.5 ns. It is also intended to extend the energy range of the neutron detector efficiency calibration to 16 MeV neutron energy.

3.2.5 Fission fragment angular distribution for $^{230,232}\text{Th}$

(J. Boldeman, R. Walsh)

The simultaneous fitting of the fission fragment angular distributions and cross sections for neutron fission of ^{232}Th is complete, but required a triple humped fission barrier.

With the restriction of a fixed shape for the fission barrier, it was possible to fit both the gross structure in the fission cross section and the details of the angular distribution, although the fitting procedure did require the use of a large number of fission bands, i.e.

*Centre d'Études de Bruyères-le-Châtel

$\bar{D}_K \approx 60$ keV. Fine structure superimposed on the gross features of the cross section, if it exists, could not be reproduced. Alternatively, fine structure can be generated if the shape of the fission barrier is allowed to change. An attempt to fit the equivalent data for neutron fission of ^{230}Th favours this second approach. However, we note that some of the experimental angular distributions are somewhat unsatisfactory and further measurements are required.

3.2.6 Measurement of fragment kinetic energies for $^{239}\text{Pu}(n,f)$

(R. L. Walsh, J. W. Boldeman, M. M. Elcombe*)

(1) Resonance Energy Region

During the last ten years a great deal of effort in a number of laboratories has been directed at discovering whether $\bar{\nu}_p$, the average number of prompt neutrons emitted per fission, is correlated with the spins of the resonances in the fission of ^{235}U and ^{239}Pu . The answer provides information on how the total energy in fission is dissipated via the different entry and exit channels available. Because of the particular nature of its fission channels, ^{239}Pu is more promising to study here than ^{235}U . However, for ^{239}Pu , the initial $\bar{\nu}_p$ results were in marked disagreement with the two major groups finding a correlation but in opposite directions. More recent data for ^{239}Pu implies that $\bar{\nu}_p$ for a $J = 0^+$ resonance is certainly higher than $\bar{\nu}_p$ for a $J = 1^+$ resonance, but the size of the effect is not clear. The data of ref. 1) implies an $2.0 \pm 0.7\%$ effect in $\bar{\nu}_p$, while the data of ref. 2) implies an $0.5 \pm 0.25\%$ effect.

The question can also be investigated by measurement of fragment kinetic energies \bar{E}_K . The most recent measurement of \bar{E}_K for $^{239}\text{Pu}(n,f)$ (ref. 3) implies an effect of $3.0 \pm 0.2\%$ in \bar{E}_K and hence in $\bar{\nu}_p$. This experiment used filtered neutron beams to isolate two energy regions near an 0^+ and a 1^+ resonance, respectively.

We have in progress a measurement of the variation of $\bar{E}_K(E_n)$ for $^{239}\text{Pu}(n,f)$ for $E_n = 0.005\text{--}0.4$ eV. The purpose is to check the results of ref. 3) and to further clarify the situation by examining the $\bar{E}_K(E_n)$ behaviour in the energy region between the first 0^+ and 1^+ resonances. Reference 3), in effect, obtained data at only two energies. Further, an important factor in obtaining the small 0.5% effect of ref. 2) is the correction that the authors make to their data to take account of the recently discovered $(n,\gamma f)$ process. In this process the excited compound nucleus emits a gamma ray before fissioning. The present measurement can produce an important, independent estimate of the contribution from this $(n,\gamma f)$ process.

A triple-axis neutron spectrometer provides a beam of monochromatic neutrons from the HIFAR reactor, via a single scatter on germanium. The fissile target is $65 \mu\text{g cm}^{-2}$ ^{239}Pu (99.97% pure) electrosprayed onto VYNS, and viewed by two heavy ion surface barrier detectors in a standard double-energy configuration. Data are recorded, event by event, on magnetic tape to provide both mass yield and kinetic energy information.

*Materials Division

¹Leonard, B. R. Jr. (1976) - private communication

²Frehaut, J. and Shackleton, D. (1973) - Proc. 3rd IAEA Symp. Phys. and Chem. of Fission, Rochester, Vol. 2, p. 201

³Toraskar, J. and Melkonian, E. (1971) - Phys. Rev. C4, 267

⁴Kolosov, N. P. et al. (1972) - At. Energiya 32, 83

(2) MeV Energy Region

Preparation are also in progress to perform a kinetic energy measurement in the MeV neutron energy region, using a neutron beam from the 3 MeV Van de Graaff accelerator. We have previously measured \bar{v}_p for ^{235}U , ^{233}U and ^{239}Pu and also \bar{E}_K for ^{235}U and ^{233}U , and have produced a theoretical prescription which reproduces the $\bar{v}_p(E_n)$ and $\bar{E}_K(E_n)$ behaviour. The \bar{E}_K measurement for ^{239}Pu remains as the one outstanding measurement needed to complete the above program. It is also important because the sole $\bar{E}_K(E_n)$ data presently available for $^{239}\text{Pu}(n,f)$ in this region (ref. 4) is in significant disagreement with the $\bar{E}_K(E_n)$ behaviour expected in terms of our established prescription.

3.3 Neutron Capture Studies

3.3.1 The joint AAEC/ORNL nuclear data project (B. J. Allen, J. Boldeman, M.J. Kenny, A. R. Musgrove, R. L. Macklin*, J. A. Harvey*, R. Taylor[†], G. Hicks[†])

Our collaboration with Oak Ridge National Laboratory in the analysis of nuclear data has continued. Neutron capture cross sections in the keV region are measured by R. L. Macklin using the 40 m flight path facility, while the 80 m and 200 m flight paths have been used by J. A. Harvey to secure high resolution transmission data for many nuclides. These data are analysed at the AAEC using locally written or modified codes.

The transmission data are analysed using a non-linear least squares, single-level fitting program to perform shape and area analysis. The capture data are analysed by Monte Carlo methods to correct for multiple scattering. A recent modification now allows the important prompt neutron scattering correction to be handled in a Monte Carlo simulation of the neutron history in the target and environs. Either single level or multilevel fitting can be selected, inelastic neutron scattering has been included and resonance-resonance interference in the γ -ray channel (e.g. where capture proceeds via a small number of exit channels as in valence capture) can be handled.

Subsequent sections discuss collaborative and local results for the following nuclides: ^{23}Na , ^{45}Sc , ^{54}Fe , $^{91,96}\text{Zr}$, $^{106,108,110,112,114,116}\text{Cd}$, ^{138}Ba , ^{139}La , ^{140}Ce , ^{176}Lu , ^{208}Pb and ^{209}Bi .

ORELA data for the isotopes ^{57}Fe , ^{141}Pr , $^{86,87}\text{Sr}$ have been analysed by R. Taylor and G. Hicks. Preliminary analysis of ^{27}Al and ^{206}Pb has also been completed. Resonance parameters for these nuclides are forwarded to the IAEA, Vienna, for inclusion in the computerised neutron data files.

3.3.2 Resonance neutron capture systematics (B. J. Allen, A. R. Musgrove)

A detailed study of the neutron capture mechanism in the threshold region (i.e. below 1 MeV neutron energy) is to be published in Advances in Nuclear Physics. Statistical and non-resonant processes are described, but the main emphasis is on a discussion of valence and doorway state models for resonance neutron capture.

A comprehensive survey of resonance radiative widths and initial and final state correlation coefficients is presented. These results are compared with detailed valence calculations using the optical model formulation. The valence model has limited success in the 3s and 3p regions and a further single particle process, uncorrelated with the reduced neutron widths, is required. This is apparent in Figure 3.1 where the correlations of valence and total radiative widths are shown. The largest radiative widths are accounted for by the valence model. However, the valence contribution is only minor for many resonances with above average radiative widths. In the 4s

*Oak Ridge National Laboratory, Oak Ridge, Tenn. 37830, USA

[†]James Cook University, Townsville, Qld. 4810

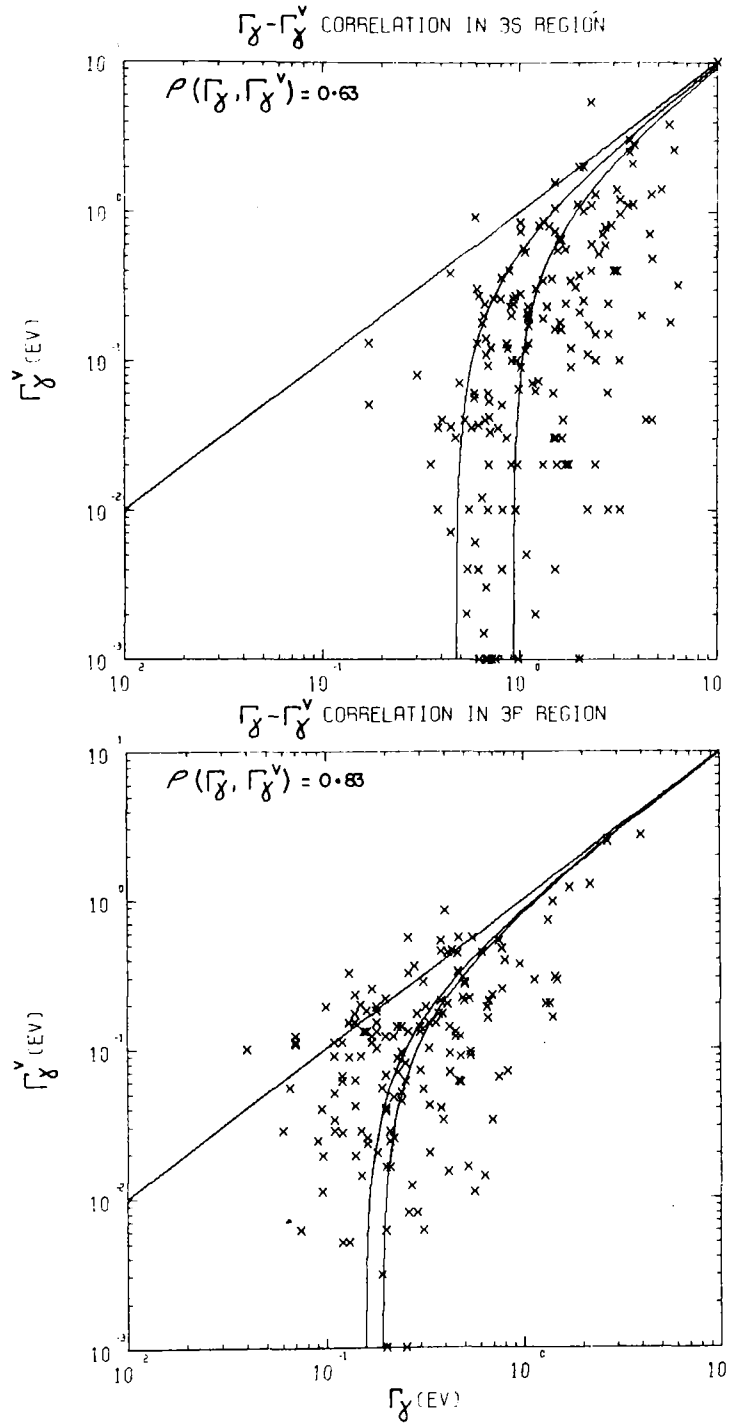


Figure 3.1 Correlation of valence and total radiative widths in 3s and 3p mass regions

region and beyond, the valence contributions are very small and an additional process is indicated which appears to be correlated with the reduced neutron widths.

These results suggest an important role for doorway states, and the contributions of particle-hole and particle-vibrator interactions are reviewed.

Overall, the capture data are found to be consistent with a significant valence contribution in the 2p, 3s and 3p regions, together with a small number of overlapping doorway states in the threshold region which carry a few per cent of the E1 strength of the giant dipole resonance.

3.3.3 Neutron sensitivity of capture γ -ray detectors (B. J. Allen, A. R. Musgrove)

Measurements of radiative widths of resonances with large neutron widths can be critically dependent on the sensitivity of the γ -ray detector to resonance scattered neutrons. This neutron sensitivity depends on the variation with energy of the capture cross sections of the detector and environs. The problem has been found to be of particular importance to the Oak Ridge capture measurements for certain nuclei where $\Gamma_n > 10^3 \Gamma_\gamma$. The problem has been resolved by the experimental determination of the neutron response function of the detector and environs, in collaboration with R. L. Macklin and R. R. Winters.

The analysis of resonance capture yields is greatly facilitated by the use of Monte Carlo methods. The observed capture yield consists of primary and multiply scattered components of both the resonance capture γ -ray yield and the γ -ray yield from the interaction of scattered neutrons.

For each neutron considered, the capture yield per incident neutron at the first collision is given by:

$$Y_1(E_1) = \frac{\sigma_c(E_1)}{\sigma_T(E_1)} [1 - T(E_1)] \quad ,$$

where σ_c , σ_s and σ_T are the neutron capture, scattering and total cross sections, respectively. The first collision probability is $1 - T(E_1)$, where $T(E_1)$ is the transmission calculated for neutrons of energy E_1 normally incident on the target. Also, from each scattering event in the target, a weighted contribution to the prompt neutron correction is estimated for those neutrons which escape the target in the direction of the capture detector or beam tube, etc. After one scattering event, we obtain:

$$Y_p(E) = \frac{\sigma_s(E_1)}{\sigma_T(E_1)} [1 - T(E_1)] T(E_2) \cdot k(E_2) \quad .$$

The factor $k(E_2)$ is the probability that the escaping neutron with energy E_2 is promptly captured in the detector or other material, and $T(E_2)$ is the probability of escaping from the target without a further collision. Additional terms also arise from multiple scattering events in the sample, leading to the escape of neutrons with reduced energy. The neutron sensitivity function $k(E)$ (Figure 3.2) is obtained from Al and S filtered beam measurements on a ^{208}Pb scattering sample.

Since the 'prompt' neutrons take some time to be captured, either in the F of the detector or Al of the beam tube, $Y_p(E)$ occurs slightly later in the γ -ray data than the primary capture yield. To save computer time, this effect has been simulated in a rough, empirical manner. It is assumed that the neutrons have to travel some minimum distance and the empirically determined average distance is allowed to have a Gaussian distribution about the mean. The constants of the random sampling method are different, depending on whether the neutron is captured in Al or F.

In the analysis of high scattering resonances, the multiple scattering capture yield is first subtracted from the observed capture yield. The calculated primary yield, together with the prompt background component is then fitted to the residual capture yield.

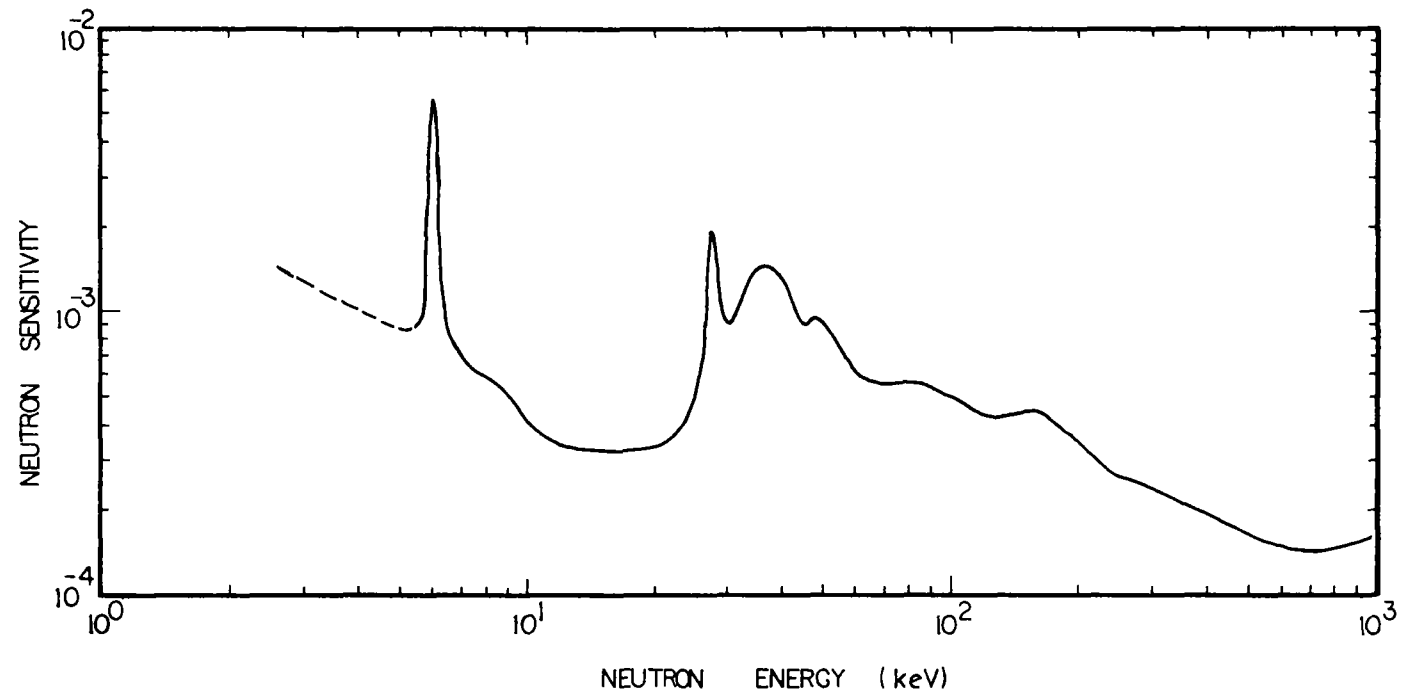


Figure 3.2 Neutron sensitivity of gamma detector as function of neutron energy

Typical fits to the 55 keV s-wave ^{28}Si resonance, the 53 keV p-wave ^{23}Na resonance and to two ^{140}Ce resonances are shown (Figure 3.3). The lower full line is the time dependent background, the broken line is the calculated prompt background and the upper full curve is the total calculated capture yield. The neutron width used for the ^{28}Si resonance is half the BNL-325 value, but recent ORELA data confirm our width.

The accuracy of the prompt background correction is found to be ~20% by fitting known radiative widths for selected resonances. The induced error in the radiative widths can sometimes be very large as Figure 3.3 illustrates.

3.3.4 Radiative capture cross sections of ^{23}Na (A. R. Musgrove, B. J. Allen)

The analysis of resonances to 600 keV was completed. The radiative width of the 2.85 keV resonance is being studied using a separate, low energy run and is awaiting a closer inspection of the prompt neutron background below the 5.9 keV Al resonance.

3.3.5 Resonance neutron capture in Sc below 100 keV (M. J. Kenny, B. J. Allen)

The neutron capture cross section of ^{45}Sc has been measured with 0.2% energy resolution in the range 2.5 to 100 keV. The average s- and p-wave radiative widths and standard deviations are $\langle \Gamma_\gamma(s) \rangle = 0.84 \pm 0.46$ eV and $\langle \Gamma_\gamma(p) \rangle = 0.5 \pm 0.3$ eV. No significant correlation is observed between the reduced neutron widths and radiative widths of the s-wave resonances.

3.3.6 Resonant and background interference in ^{54}Fe capture

(B. J. Allen, A. R. Musgrove, W. K. Bertram)

The initial state correlation coefficient for ^{54}Fe ($\rho(\Gamma_{\lambda n}^0, \Gamma_{\lambda \gamma}) = 0.94$), is related to the distant resonance component of the non-resonant capture cross section:

$$\sigma_{\gamma\mu}(\text{BG}) = \frac{\pi^2}{4} \cdot \frac{2.608}{\sqrt{E_n}} \cdot 10^6 \cdot g \cdot S_0 \cdot S_{\gamma\mu} \cdot \rho_{I\mu}(\Gamma_{\lambda n}^0, \Gamma_{\lambda \mu}) ,$$

where S_0 , S_γ are the neutron and radiative strength functions, E_n is in eV and μ designates the final state. For the ground state ($\mu=0$), $S_{\gamma 0} \approx 0.62 \times 10^{-4}$, $S_0 = 8.6 \times 10^{-4}$ and $\rho_{I0} \sim \rho_I = 0.94$, since 75% of the valence strength is found in the ground state transition. For ^{54}Fe , $\sigma_{\gamma 0}(\text{BG}) = \frac{0.32}{\sqrt{E_n}} = 2$ barn at thermal, a value comparable to the measured thermal capture cross section of 2.25 barn. Since 1.74 barn is accounted for by the tail of the 7.7 keV resonance ($\Gamma_\gamma = 1.9$ eV), this background estimate is at best a factor of four too large.

Various calculations, which are particularly sensitive to the potentials used, give thermal background capture cross sections for ^{54}Fe varying from 0.1 to 1.0 barn. Accordingly, a significant background cross section is expected in ^{54}Fe which will interfere with the partial resonance capture cross sections.

We previously reported asymmetric s-wave capture resonances at 130, 148 and 174 keV with low energy tails and these have now been analysed in detail.

Since valence capture is expected to allow the observation of resonance-direct interference in the total capture cross section, it will also result in interference between s-wave resonances. It is therefore necessary to calculate the valence γ -ray cross section using a multilevel formalism. Results for resonances at 129.6, 146.8, 174.4 and ~184 keV are shown in Figure 3.4. The calculated curves were obtained for $\sigma_\gamma(\text{BG}) = 0$. The multiple scattered component has been subtracted (lower histogram) and the prompt background component (broken line) is added to the primary γ -ray yield. All resonance cross sections are well reproduced, although the energy of the 184 keV resonance is ~8 keV below the total cross section value.

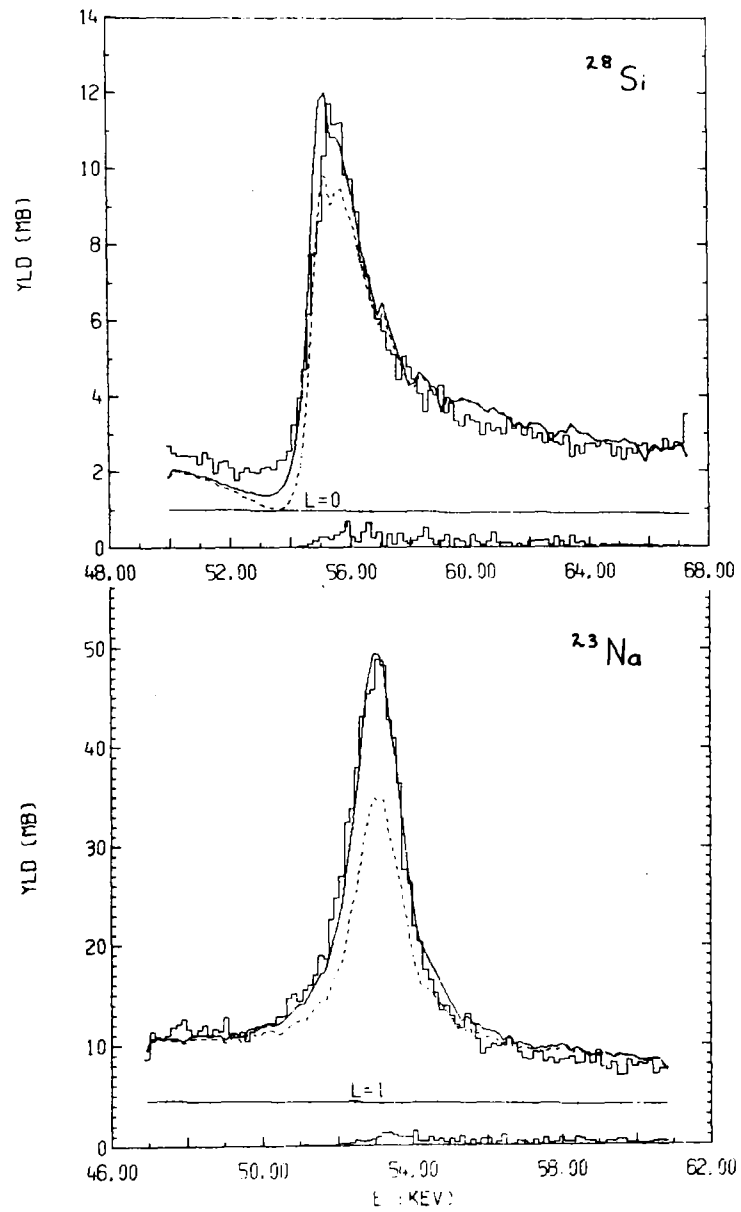


Figure 3.3 Prompt background influence on symmetry of capture resonance

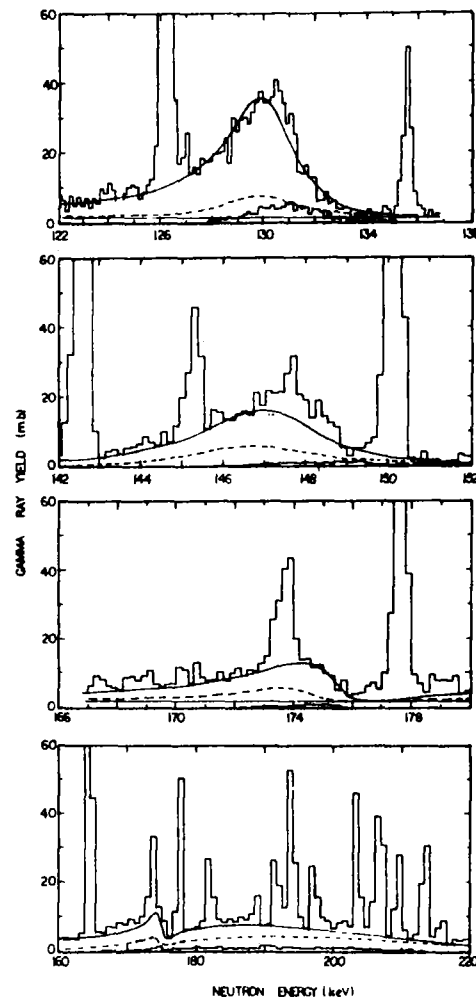


Figure 3.4 Asymmetric resonances: interference between valence channels and broad resonances

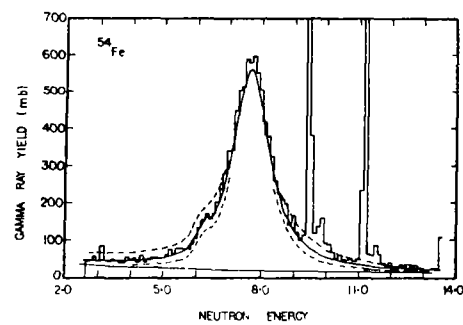


Figure 3.5 7.7 keV ^{54}Fe resonance fit and thermal background cross section

The asymmetries at 129.6, 146.8 and 174.4 keV are accounted for by interference with the broad ($\Gamma_n = 40$ keV) resonance at 184 keV. This resonance exhibits an asymmetry opposite to that of the lower energy resonances, a result which is inconsistent with a resonance-direct interference hypothesis. The estimated valence width of 10 eV accounts for ~90% of the total radiative width of this resonance and supports the validity of the single capture channel, multi-level calculation.

After subtraction of a 25% multiple scattering contribution, the 7.7 keV resonance is found to be quite symmetric (Figure 3.5). (The peak at 6 keV results from the capture of scattered neutrons by the 5.9 keV resonance in the aluminium beam tube and detector assembly.) The expected line shapes for a thermal background cross section of 0.3 barn (for positive and negative amplitudes) are shown for comparison. Since this resonance is estimated to be completely valence in character, an upper limit of ≤ 0.1 barn can be set for the thermal background cross section.

3.3.7 Resonance parameters for ^{89}Y (J. Boldeman, B. J. Allen, A. R. Musgrove)

The ORELA neutron capture data for ^{89}Y has been analysed to 47 keV. The average radiative widths determined were $\langle \Gamma_{ys} \rangle = 0.115 \pm 0.015$ eV and $\langle \Gamma_{yp} \rangle = 0.307 \pm 0.031$ eV. The most interesting feature of the data was the strong correlation $\rho(\Gamma_n^1, \Gamma_Y) = 0.71 \pm 0.025$ for the 13 p-wave resonances in the data set, and the significant difference in the average s- and p-wave radiative widths. The success of the valence model in accounting for both of these features provides the first evidence of the applicability of the valence model in the 3p region to odd-A target nuclei.

3.3.8 Resonance parameters of ^{91}Zr and ^{96}Zr (A.R. Musgrove, B.J. Allen, J. Boldeman)

Transmission data at 80 m and 200 m stations of ORELA were analysed to 20 keV to obtain an essentially complete set of resolved resonance parameters for ^{91}Zr . The average resonance parameters obtained were as follows:

$$\langle D \rangle_s = 640 \pm 120 \text{ eV}, \quad 10^4 S_0 = 0.36 \pm 0.10, \quad \langle \Gamma_Y \rangle_s = 140 \pm 8 \text{ meV}$$

$$\langle D \rangle_p = 300 \pm 50 \text{ eV}, \quad 10^4 S_1 = 5.7 \pm 1.0, \quad \langle \Gamma_Y \rangle_p = 220 \pm 12 \text{ meV}$$

The correlation between Γ_n^1 and Γ_Y , $\rho(\Gamma_n^1, \Gamma_Y) = 0.41$, was attributed to valence neutron processes.

For ^{96}Zr , two 80 m runs were analysed to 100 keV to give the following average resonance parameters:

$$\langle D \rangle_s = 8 \pm 2 \text{ keV}, \quad 10^4 S_0 = 0.21 \pm 0.10, \quad 10^4 S_1 = 7.4 \pm 2.0.$$

3.3.9 Resonance parameters for the even-A isotopes of Cd (A.R. Musgrove, B.J. Allen)

The ORELA (n, γ) data for all the even-A Cd isotopes were analysed and average resonance parameters obtained are given in Table 3.3. This is the first published resonance parameter information for the neutron deficient isotopes $^{106}, ^{108}\text{Cd}$. We identified several p-wave resonances with $g=2$ among the 's-wave' resonances recommended by Liou et al. (1974)*. The new values for both $\langle D \rangle_s$ and S_1 are increased over the previous values.

The average s-wave radiative width decreases strongly with decreasing neutron binding energy contrary to the almost constant trend reported by Liou et al. The p-wave radiative widths are substantially greater than Γ_{ys} since most of the low lying states are positive parity s- and d-wave levels.

Both s- and, to a smaller extent, the p-wave neutron strength function decrease as the neutron number increases. This is remarkably well accounted for by replacing the absorptive

*Liou, H. I., Hacken, G., Rhan, F., Rainwater, J., Slagowik, M. and Makofske, W. (1974) - Phys. Rev. C10, 706

TABLE 3.3

AVERAGE RESONANCE PARAMETERS FOR THE CADMIUM ISOTOPES

	^{106}Cd	^{108}Cd	^{110}Cd	^{112}Cd	^{114}Cd	^{116}Cd
$\langle D \rangle_s$ s-wave level spacing	135±35	120±30	155±20	190±25	235±35	390±90
$\langle D \rangle_s$ from Liou et al. (1974)			174±18	137±8	183±29	164±38
$\langle \Gamma_Y \rangle_s$	155±15	105±10	71±6	77±5	53±4	47±4
S.D.	~30	~20	~16	~15	~5	~9
$10^4 S_0$	1.0±0.35	1.16±0.40	0.28±0.07 ^{a)}	0.50±0.10	0.64±0.16	0.16±0.05
$\langle D' \rangle_p$ observed uncorrected p-wave spacing	113±30	127±30	87±20	90±20	145±20	270±50
$\langle \Gamma_Y \rangle_p$ (from resonances)			84±13	96±25	82±7	85±8
S.D.			~25	~20	~15	~16
$\langle \Gamma_Y \rangle_p$ (from cross section fit)	175±25	125±20	80±15	90±20	70±10	70±10
$10^4 S_1$ from Liou et al. (1974)	5.0±1.5	4.75±1.25	4.0±0.9	4.4±1.0	3.5±1.0	2.8±0.8
$10^4 S_1$			2.8±0.6	2.5±0.5	3.2±1.0	
$\langle \sigma(n, \gamma) \rangle$ 30 keV	480±50	450±70	250±30	233±20	158±25	92±12

a) Above 3 keV; below 3 keV $10^4 S_0 \approx 0.73$

part W , of the optical model potential by one containing an isospin dependent term $W = W_0 - W_1 (N-Z/A)$ as was done by Tellier and Newstead*.

Figure 3.6 shows the fit to S_0 for the Zr, Cd and Te isotopes using the Tellier-Newstead potential and the predicted p-wave neutron strength function for Cd and for the important Pd isotopes.

3.3.10 Neutron capture in ^{139}La (A. R. Musgrove, B. J. Allen)

The ORELA (n, γ) data were analysed to 15 keV giving the following average resonance parameters:

$$\langle \Gamma_{\gamma} \rangle_s = 55 \pm 6 \text{ meV}, \langle \Gamma_{\gamma} \rangle_p = 40 \pm 7 \text{ meV} \text{ and } 10^4 S_1 = 0.30 \pm 0.10$$

The s-wave resonances decay strongly to final f-wave states via a postulated 2p-1h doorway mechanism; however there is no evidence that the strengths of these decays are correlated with the neutron width of the initial state.

3.3.11 Neutron capture in ^{138}Ba and ^{140}Ce (A. R. Musgrove, B. J. Allen)

The previous data for ^{138}Ba have been re-analysed in the light of the new information on the prompt background correction. For both these nuclides the correction amounts to up to ~80% of the observed yield for the large s-wave resonances. It is now apparent that much of the large reported correlations $\rho(\Gamma_n^0, \Gamma_{\gamma})$ for these nuclei can be attributed to the prompt scattered neutrons. Previously reported capture cross sections for these nuclei are now much reduced, a result which has important astrophysical implications.

3.3.12 Gamma rays from keV neutron capture in lanthanum (M. J. Kenny, B. J. Allen)

The neutron capture mechanism for γ -ray transitions to final states with large angular momenta has been investigated for ^{139}La . Neither the statistical nor valence models could account for the anomalous γ -ray intensities and a two-particle, one-hole mechanism was invoked to explain the data. Transitions to the 0^- , 7^- states were not observed and an upper limit of 20% was deduced for the d-wave contribution to the capture cross section.

Additional support is therefore given to the argument that neutron capture to the final f-wave states proceeds via a 2p-1h doorway. If the annihilation of the p-h pair leaves a neutron in the $f_{7/2}$ orbit coupled to an unperturbed core, final state correlations are expected between the (d,p) intensities and the corresponding γ -ray intensities. However, keV capture occurs through s-, - and d-wave channels and thus γ -ray intensities need to be reduced by the appropriate weighting factors. Unfortunately, intensities to the 0^- , 7^- states are only upper limits and those to the 1^- , 6^- states have very large errors. These states cannot therefore be included in a correlation calculation even though they comprise the strongest and weakest (d,p) intensities.

These problems can be avoided by considering the relative intensities of transitions to pairs of like spin states which have been split by the $|\pi(1g_{7/2})\rangle$ and $|\pi(2d_{5/2})\rangle$ quasi-proton states. The state vectors are linear combinations of these states coupled to the $f_{7/2}$ neutron, i.e.

$$|JM\rangle_i = \alpha_i |\pi(1g_{7/2}) \nu(2f_{7/2}) : JM\rangle + \beta_i |\pi(2d_{5/2}) \nu(2f_{7/2}) : JM\rangle$$

Since the ground state of ^{139}La is $|\pi(1g_{7/2})\rangle$, the (d,p) spectroscopic factor is proportional to α^2 . Consequently, the relative intensities of (d,p) transitions to the states $|JM\rangle_i$ and $|JM\rangle_2$ reflect the single particle nature of these states. If the p-h interaction in resonance

*Tellier, H. and Newstead, C. (1971) - Knoxville Conference. CONF-710301, Vol. 2, p. 680

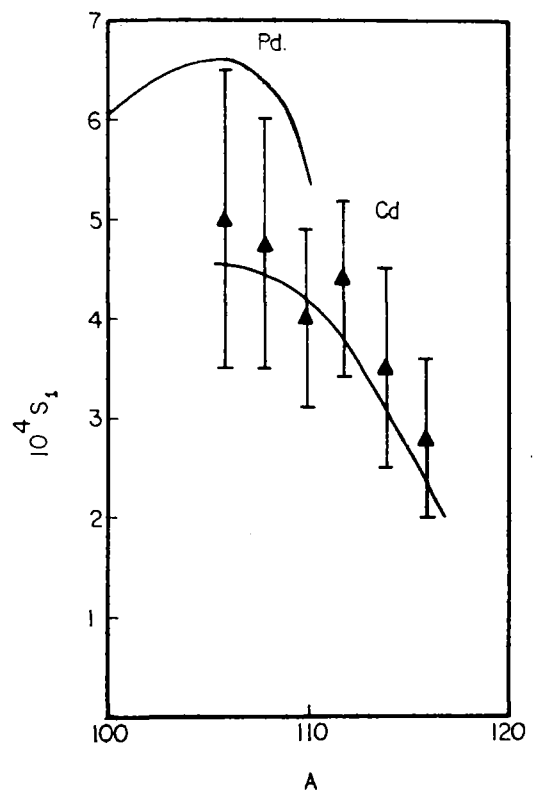


Figure 3.6 (a) p-wave strength functions for cadmium isotopes

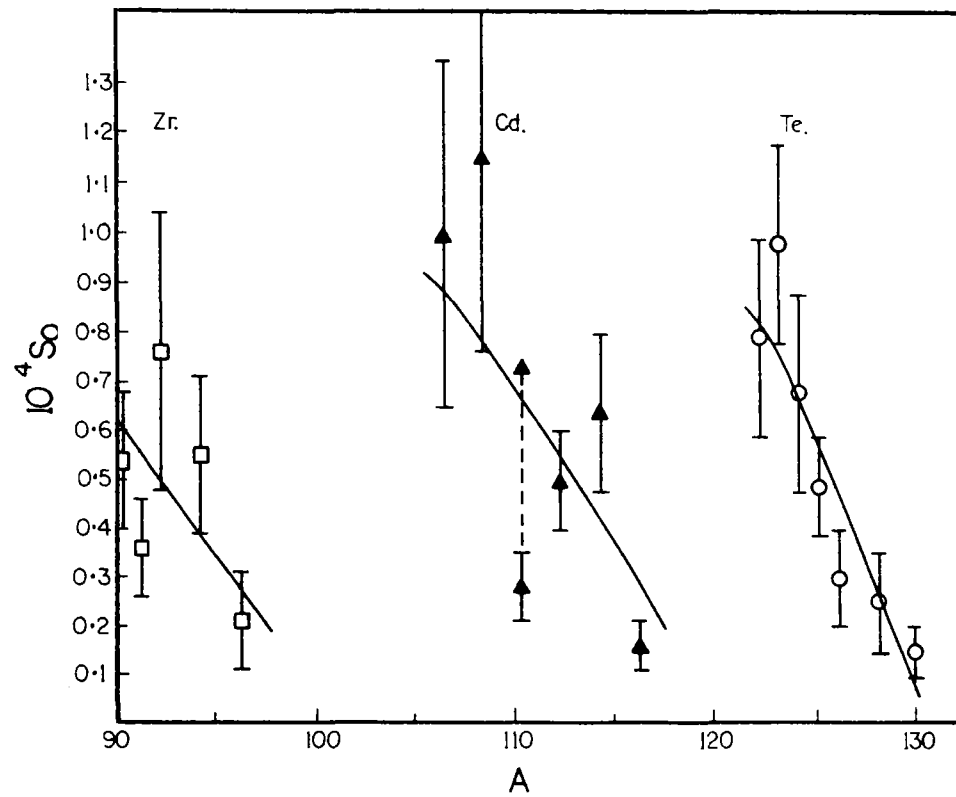


Figure 3.6 (b) s-wave strength functions for Zr, Cd and Te isotopes

capture leaves the core in an unperturbed state, then the (d,p) and (n, γ) intensities will be correlated. However, since the excitation energy of the $2d_{5/2}$ proton orbit in ^{139}La is only 166 keV, the core may well be left perturbed and in this case, intensities will therefore be anti-correlated with the (d,p) strength.

Ratios for (d,p) thermal and averaged keV intensities are found to be comparable for the 2^- state, but appear anti-correlated for the 3^- state. These results cannot be explained on the statistical model.

In average capture, resonances with both unperturbed and excited target state configurations may be present which favour transitions to similar components in the 2^- and 3^- final states, respectively. Capture γ -ray spectra from single resonances are needed to confirm that pairs of transitions to the 2^- and 3^- states are either both correlated, or both anti-correlated, with the (d,p) strengths since the thermal data suggests that this is not the case.

3.3.13 Branching ratio of ^{176}Lu at astrophysical energies

(J. R. de Laeter*, B. J. Allen, G. C. Lowenthal[†])

Estimates of the age of the universe can be made from measurements of the expansion of the universe, the evolution of globular clusters and by nucleocosmochronology. The major processes involved in the latter occur during a supernova (the rapid r-process) or in stellar interiors where the capture rate is slow compared to the decay rate of product nuclides (the slow s-process).

The only true s-process chronometer is the ^{176}Lu - ^{176}Hf pair. Lutetium-176 is formed by $^{175}\text{Lu}(n,\gamma)$ and decays to ^{176}Hf with a half-life of 3.6×10^{10} years. The Schumann-Wasserburg formalism can therefore be applied if the branching ratio to the long-lived ground state is known at astrophysical neutron energies.

A measurement of this branching ratio was therefore undertaken at the 3 MeV Van de Graaff accelerator. The $^7\text{Li}(p,n)$ reaction at threshold is a prolific source of 30 keV neutrons which were used to irradiate a pure sample of Lu_2O_3 (97.4% ^{175}Lu) and a thin Au foil. A cadmium shield was used to absorb thermalised neutrons. The 88 keV γ -ray from the $^{176\text{m}}\text{Lu}$ isomer decay ($t_{1/2} = 3.69$ hours) was detected by a Ge(Li) spectrometer and the Au activity measured in a 4π β - γ coincidence counter. A ground state branching ratio of 0.31 ± 0.06 was found for 30 keV neutrons.

3.3.14 Radiative capture cross section of ^{208}Pb (A. R. Musgrove, B. J. Allen)

Recently Macklin, Halperin and Winters (1977)¹ published high resolution ORELA data on resonance capture in ^{208}Pb below 850 keV. Although an approximate correction to the data was made for prompt neutrons scattered into the capture detector, this has now been found to be entirely inadequate for thick samples, such as the present one. The Monte Carlo program was recently modified to handle the prompt background problem and the ^{208}Pb data have now been re-analysed. Some of the important resonances previously reported, are now seen to have extremely small capture widths since the prompt background component accounts for ~100% of the observed yield. Most importantly for astrophysical calculations, the resonances at 68.3, 68.7 and 77.6 keV are in this category. Figure 3.7 gives the fit to the data for these resonances. Accordingly, the Maxwellian averaged cross section in the region of stellar neutron capturing temperatures (<100 keV) is now less than half the Macklin et al. value.

*Western Australian Institute of Technology

[†]Instrumentation and Control Division

¹Macklin, R. L., Halperin, J. and Winters, R. R. (1977 - Phys. Rev. (in press))

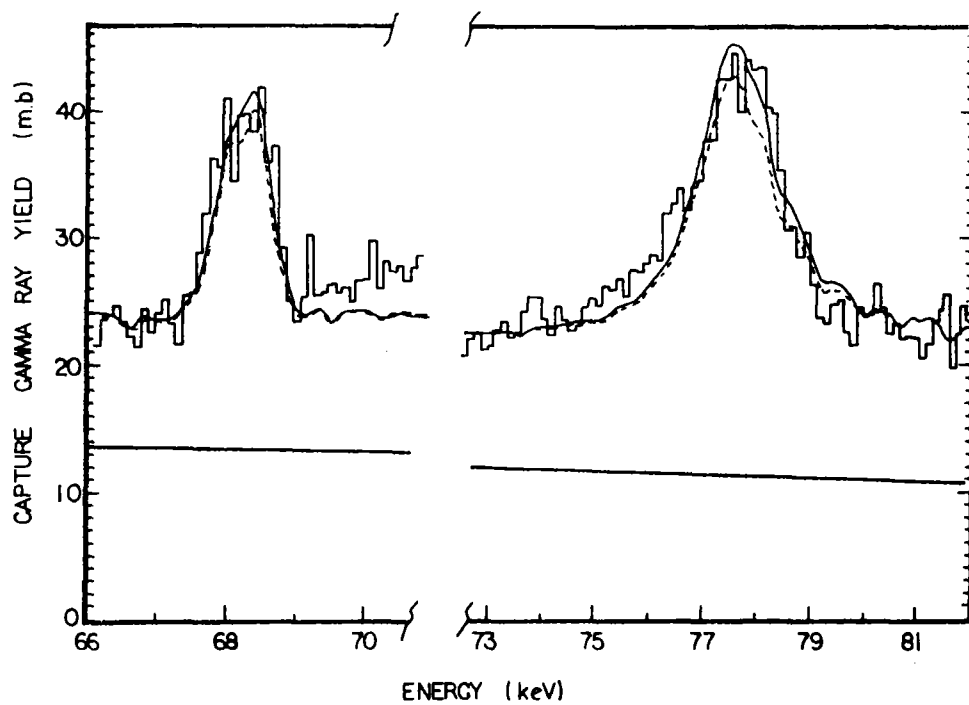


Figure 3.7 Fit to a doublet at 68 keV and the 78 keV $1/2^-$ resonance in ^{208}Pb

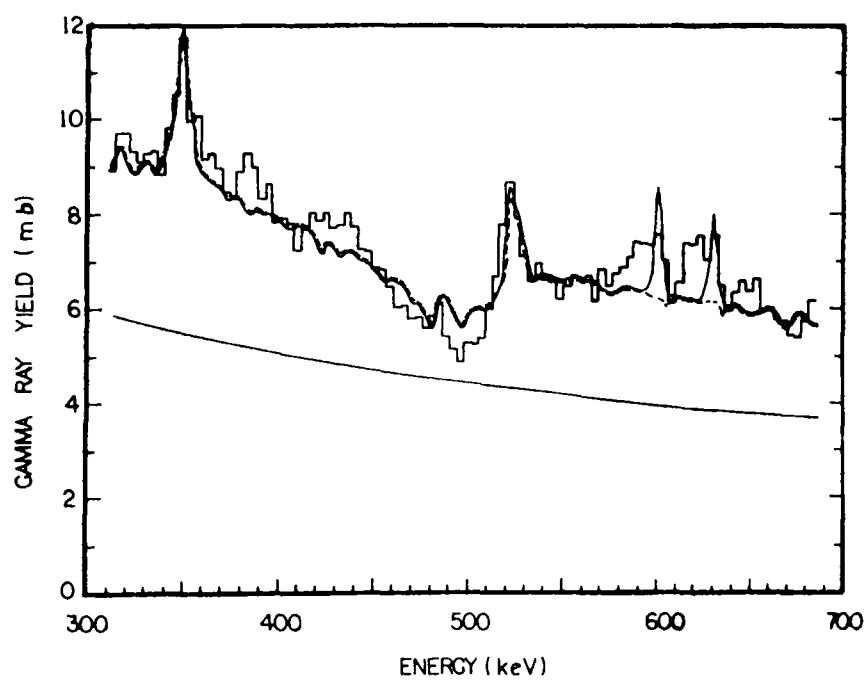


Figure 3.8 Fit to 500 keV dip in ^{208}Pb using $\Gamma_n = 60$ keV

TABLE 3.4

 ^{208}Pb RESONANCE PARAMETERS (re-analysed)

E (keV)	$g\Gamma_n\Gamma_\gamma/\Gamma$ (meV)	Γ_n (eV)	J^π	Γ_γ (meV)	E (keV)	$g\Gamma_n\Gamma_\gamma/\Gamma$ (meV)	Γ_n (eV)	J^π	Γ_γ (meV)
43.30	25±4				357.5	394±160			
47.28	38±3				405.5	≤25	(200)		
68.30	≈20	120±40		<50	419.8	≤25	(140)		
68.73	≈50	220±80		<100	486.0	300±250	(2400)	$(1/2^-)$	300±250
(70.15)	45±15				500.0	≤100	(60000)	$1/2^+$	<100
(70.87)	36±12				508.5	≈100	(165)	$(3/2^-)$	
77.8	150±100	1300±200	$1/2^-$	150±100	524.5	1480±800	(4680)	$(5/2^+)$	400±300
86.55	<0.010	<40			564.0	≤100	(424)		
116.9	30±25	250±50	$1/2^-$	30±25	567.5	≤100	(37)		
130.1	360±20	(23)			573.0	650±150			
166.5	210±25				607.5	≤100	(113)		
168.1	160±40	(18)			610.0	≤100	(170)		
168.6	66±13	(24)			684.0	260±200	(269)	$(3/2^+)$	
169.2	222±30	(20)			700.5	360±260	(271)	$(5/2^-)$	
193.3	394±30	(10)			720.0	1160±180	(130)		
266.7	688±150				721.9	560±130	(3798)	$(5/2^+)$	280±70
269.8	195±80	(119)	$(3/2^-)$	100±40	735.5	4250±350	(179)	$(5/2^-)$	1430±120
274.8	312±60				761.0	4890±350	(1517)	$(5/2^+)$	1630±120
276.7	157±80	(318)	$(1/2^-)$	157±80	769.5	3400±200	(50)		
325.2	100±80	(123)	$(3/2^-)$	50±40	783.1	6990±420	(110)	$(5/2^-)$	2380±140
349.5	≤50	(4870)	$(3/2^+)$	≤50	810.5	3650±1000	(8463)	$(5/2^+)$	1215±350
					823.5	3010±450	(183)	$(5/2^-)$	1000±150

Table 3.4 lists the re-analysed data including spin, parity and neutron width information from the recent data of Fowler et al. (1976)². Our fits to the resonances at 77.6 and 116.9 keV indicate that they are both $1/2^-$. The other spin and parity assignments are open to some doubt (Fowler 1977³).

Table 3.5 gives the Maxwellian averaged capture cross sections for temperatures kT below 100 keV.

Figure 3.8 shows the fit to the 500 keV s-wave dip and environs using $\Gamma_n = 60$ keV for this resonance. The time dependent background decreases approximately as $E^{-0.7}$. The prompt background is shown as the broken lines and the total calculated capture yield is the upper full line.

TABLE 3.5
MAXWELLIAN AVERAGED NEUTRON CAPTURE BY ^{208}Pb

kT (keV)	$\frac{\sigma \cdot v}{v_T}$ (mb)
10	0.04±0.01
20	0.18±0.03
30	0.25±0.05
40	0.29±0.08
50	0.31±0.10
60	0.31±0.10
70	0.31±0.10
80	0.30±0.10
90	0.29±0.10
100	0.28±0.10

3.3.15 Neutron resonance spectroscopy on ^{209}Bi (A. R. Musgrove)

Analysis of the 200 m ORELA transmission data for ^{209}Bi was completed to 270 keV bombarding energy. Approximately 25% of the expected neutron strength of a $(g_{9/2} \otimes 4^+)$ particle-vibrator doorway state was identified. The doorway was centred near 300 keV with $\Gamma^\downarrow \approx 350$ keV.

The average s-wave level spacing is $\langle D \rangle_s = 4.5 \pm 0.6$ keV after correcting for missed levels. The s- and p-wave neutron strength functions are respectively, $10^4 S_0 = 0.65 \pm 0.15$ ($E < 170$ keV); $10^4 S_1 = 0.25 \pm 0.07$ ($E < 60$ keV). Both strength functions show evidence of energy dependent structure.

3.3.16 s-wave neutron capture in ^{209}Bi (A. R. Musgrove, B. J. Allen)

The recent capture data of Macklin and Halperin (1976) for ^{209}Bi showed strong correlations between s-wave radiative widths and the reduced neutron widths ($\rho(\Gamma_n^0, \Gamma_\gamma) > 0.6$). Also the s-wave radiative widths were a factor of five greater than the p-wave widths. In the absence of valence

²Fowler, J. L., Johnson, C. H. and Hill, N. W. (1976) - Bull. Am. Phys. Soc. 21, 537

³Fowler, J. L. (1977) - private communication

neutron transitions, these measurements were particularly difficult to reconcile with theory, especially since the doorway state observed in the neutron channel has almost no intrinsic radiation associated with it.

To see whether prompt neutron background could cause the large widths and correlations, the ^{209}Bi data were re-analysed using the Monte Carlo method to correct for prompt scattered neutrons. Table 3.6 gives the revised resonance parameters for s-wave neutron capture below 100 keV and Table 3.7 gives Maxwellian averaged capture cross sections which include all p- and d-wave resonances as found by Macklin and Halperin (1976)¹ and also by Musgrove and Harvey (1977)². The observed correlation coefficient is now $\rho(\Gamma_n, \Gamma_\gamma) = 0.2 \pm 0.5$, consistent with zero (although with a large error). The new s-wave weighted average radiative width is $\langle \Gamma_{\gamma s} \rangle = 53 \pm 15$ meV. By comparison, the average p-wave radiative width is found to be $\langle \Gamma_{\gamma p} \rangle = 22 \pm 5$ meV.

TABLE 3.6
AMENDED s-WAVE PARAMETERS FOR ^{209}Bi

E (eV)	$g\Gamma_n\Gamma_\gamma/\Gamma$ (meV)	Γ_n (eV)	g	Γ_γ
5.115	32±2	5.74	0.55	59±6
12.11	51±10	259	0.45	112±24
15.51	48±6	129	0.45	106±15
7.08	36±12	24.1	0.45	80±30
33.33	46±26	273	0.45	102±50
45.62	30±20	152	0.55	55±40
49.87	19±9	8.6	(0.5)	38±20
52.73	5±5	24.7	(0.5)	10±10
53.71	12±7	36.6	(0.5)	24±14
61.58	41±15	93	0.45	91±30
69.16	55±40	470	0.55	100±70
72.61	17±8	21.5	0.45	37±17
81.63	12±5	172	0.55	22±10
84.26	78±30	20.6	(0.5)	158±60
85.19	13±13	238	(0.5)	26±26
95.35	18±12	400	0.45	40±25

TABLE 3.7
MAXWELLIAN AVERAGED CAPTURE CROSS SECTIONS FOR ^{209}Bi

kT (keV)	10	20	30	40	50	60	70	80	90	100
$\frac{\sigma \cdot v}{v_T}$ mb	7.7±0.8	4.1±0.5	2.8±0.5	2.1±0.3	1.7±0.2	1.4±0.2	1.2±0.2	1.1±0.2	1.0±0.2	0.9±0.2

¹Macklin, R. L. and Halperin, J. (1976) - Phys. Rev. C14, 1389

²Musgrove, A. R. de L. and Harvey, J. A. (1977) - to be published

3.4 Nuclear Techniques of Analysis

3.4.1 New beam line facilities (L. H. Russell, M. D. Scott, A. van Heugten, H.G. Broe)

A new beam line has been installed with provision for two sample chambers in a shielded area to minimise background radiation from other parts of the 3 MeV accelerator target areas. The beam line has been equipped with a quadrupole focusing magnet, selectable water-cooled aperture, beam profile monitor, pneumatically operated beam stop and turbomolecular pumping system. One of the sample chambers is equipped with a 1 metre long, computer driven sample changer for automated analysis of samples in a vacuum of the order of 1 mPa. The other chamber to be installed will be an ultra high vacuum chamber for use in the study of surfaces requiring special care to avoid contamination.

Three types of detector system are used simultaneously for detection of charged particles (silicon detector), gamma rays (lithium drifted germanium detector) and X-rays (lithium drifted silicon detector). Electron flood and electron suppression systems are also used, the former to prevent charging of insulating targets. New on-line computer programs (in FOCAL language) provide for data collection and analysis, as well as sample positioning. Data and operating programs can also be transferred to and from the IBM 360. Increased use is being made of these facilities for multi-sample analyses during unattended overnight accelerator runs.

3.4.2 Proton induced X-rays (P. Duerden, D. Cohen*, E. Clayton)

Proton induced X-ray spectra have been used in a number of exploratory measurements to assess the usefulness of the technique and to assist in the development of the necessary equipment and data analysis techniques. The characteristic X-ray spectrum for each element consists of a bremsstrahlung background with individual X-ray peaks ($K_{\alpha,\beta}$, $L_{\alpha,\beta,\gamma}$, $M_{\alpha,\beta}$) superimposed on it. Figure 3.9 shows a typical spectrum (NaWO_4) and highlights some of the problem areas (escape peaks, target charging, pulse pile-up and the need for low energy fitting) that arise in spectrum analysis.

Escape peaks: When an X-ray (energy E) enters the silicon detector, it can interact with a silicon atom to produce a silicon K_{α} X-ray of energy 1.74 keV. This may escape from the detector and leave an energy $E - 1.74$ keV to be detected. The probability for escape peak production at different energies has been measured.

Target charging: An insulated target becomes charged under proton bombardment and the resulting electric field accelerates secondary electrons to produce bremsstrahlung radiation which could be many times greater in intensity than that produced by conducting targets. This effect is removed either by flooding the target with electrons from a heated carbon filament or by doping the target material with carbon powder so that the target is no longer insulated. Figure 3.10 shows the effect of electron flood.

Pile-up: Pulse pile-up gives rise to sum peaks which can interfere with, and be of comparable magnitude to genuine peaks from trace elements. For example, thorium analysis is more difficult when iron is present in the sample, since the energy of the thorium L_{α} X-ray is exactly twice that of the iron K_{α} X-ray.

Filters: Perspex layers (1.5 mm thick) are placed between the target and the detector to preferentially absorb low energy X-rays. High energy X-ray peaks can then be enhanced with respect to the low energy end of the spectrum by an increase in proton beam current. The lowering of the count rate in the low energy peaks also reduces sum peak effects. Figure 3.11 shows this effect when a Perspex filter is used in the analysis of a uranium ore sample.

* Australian Institute of Nuclear Science and Engineering

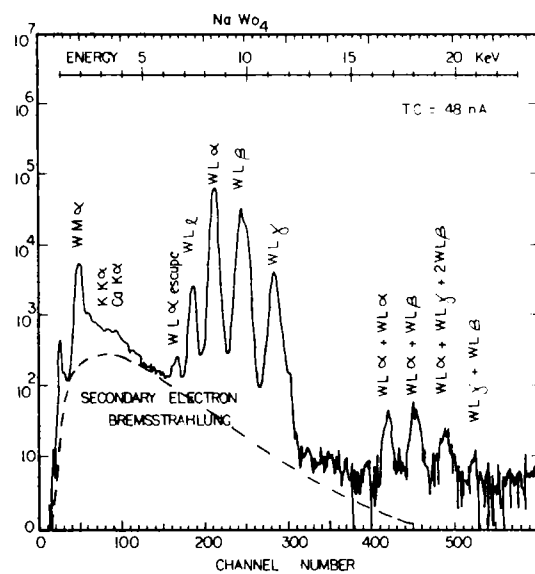


Figure 3.9 Typical raw PIXE spectrum

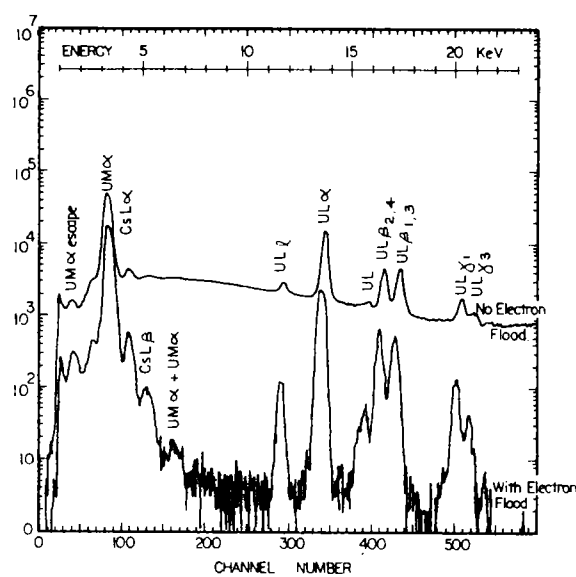


Figure 3.10 PIXE spectrum using electron flood technique

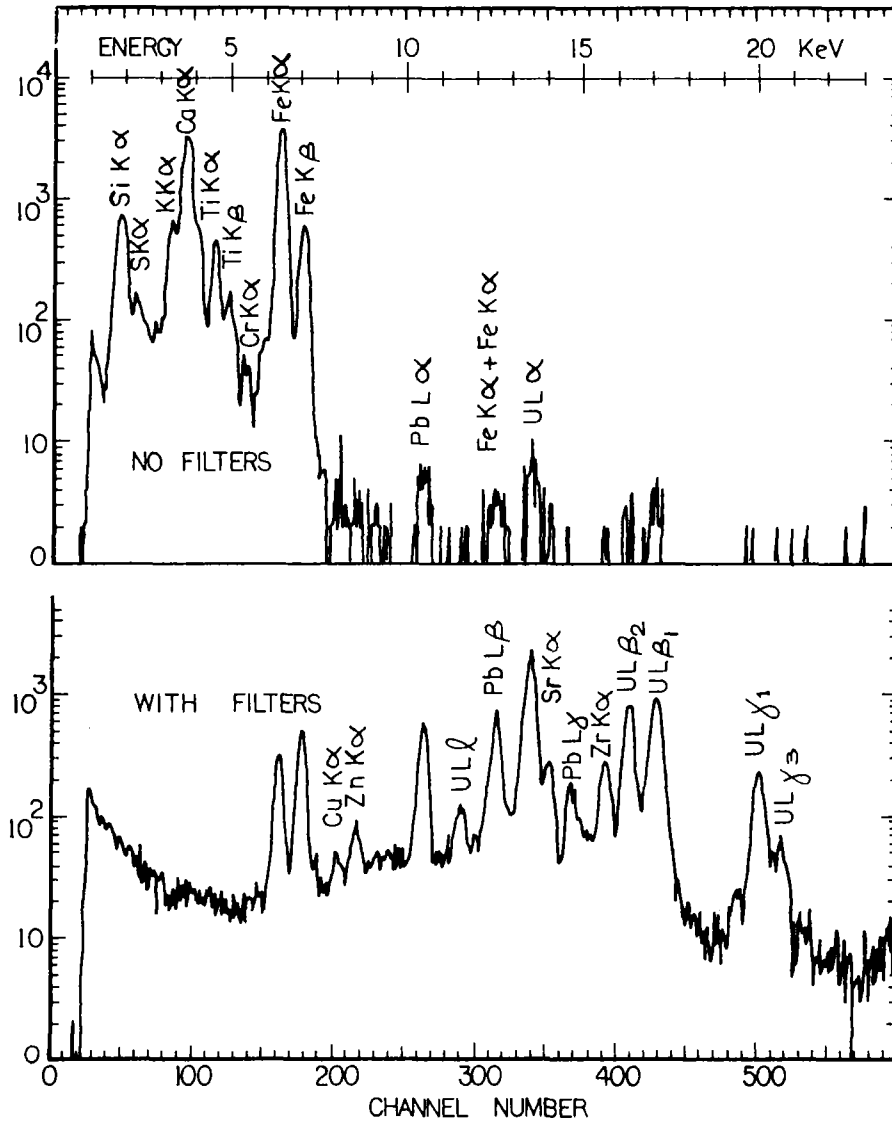


Figure 3.11 Filtering of PIXE spectrum to remove sum peaks

The spectrum obtained when the filter is used has no observable sum peaks.

Three computer codes have been developed to analyse the experimental spectra. The experimental data are fitted in these codes by an exponential function (modelling the bremsstrahlung background) with Gaussian functions (modelling the individual X-ray peaks) superimposed. The first code smooths the experimental data and calculates the background spectrum; this program will be extended to cover pulse pile-up removal, escape peak removal and the effect of filters. The second code is a least squares fitting calculation which is used to estimate peak positions and intensities of the various transition lines (e.g. K_{α} to K_{β} ratios) for reference standards. This data provides a library for the third program. The latter code analyses the spectrum from a multi-element sample and will eventually calculate the concentrations of each of the elements present. Corrections will have to be made to account for varying X-ray product cross sections with energy, absorption of the emitted X-ray and the presence of all elements within the sample matrix.

Figure 3.12 shows the background fitting procedure in the first code and the Gaussian fit to the spectrum after removal of this background.

3.4.3 Artefacts (P. Duerden, R. J. Bird)

Simultaneous measurements of X-rays and scattered protons have been used to study two metal artefacts submitted by Dr. N. Barnard (Department of Far Eastern History, Australian National University).

Measurements at a number of different positions on a bronze head showed the presence of many elements, some of which can be attributed to surface corrosion products. There was also considerable variation in composition from position to position. However, all positions showed significant levels of Fe and Zn as well as lighter metals, suggesting that the artefact was made from a modern casting alloy.

Similar measurements were made for a Chinese coin-ingot, circa 19th century, indicating clearly that the coin is a silver-copper alloy rather than pure silver. The backscattering spectra showed the presence of carbon in the black inlay, along with oxygen, silicon and other elements. Variations in the backscattering spectra and X-ray spectra from position to position gave information on the nature of the inlay material and of areas of surface damage.

3.4.4 Tin on glass (M. D. Scott, L. H. Russell, J. R. Bird, D. G. Owen*)

Tin oxide layers are sometimes applied to bottle glass during manufacture to provide suitable bonding for layers of plastic. Proton or alpha particle backscattering are ideal for the difficult determinations of thickness and uniformity of the layers that are produced. Typical alpha backscattering spectra are shown in Figure 3.13, taken at different positions along the threaded portion of a coated bottle.

The amount of tin present can be readily determined in five minutes measuring time and used to define a profile of tin oxide from the lip of the bottle across the thread to the body of the bottle. Anomalous results are observed when the beam strikes a portion of the thread which is at a very different angle to normal, but the visibility of the beam spot makes it easy to avoid such anomalous positions.

3.4.5 Aluminium (M. D. Scott)

Additional measurements have been made of the aluminium on the surface of silica which had been used to getter molten germanium (A. Tavendale, I&C Division). Using electron flood

*ACI Technical Centre Pty. Ltd.

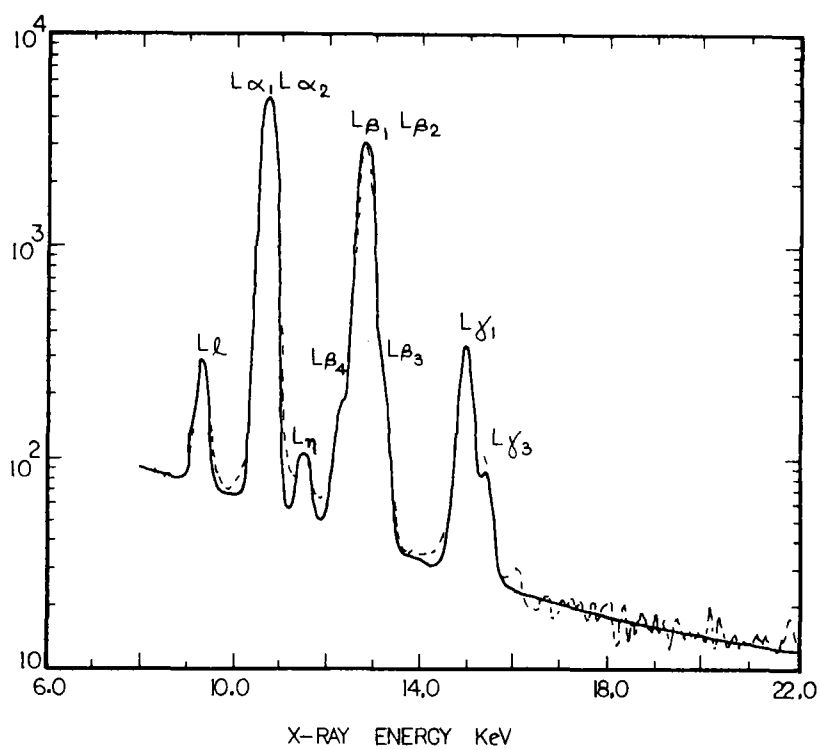
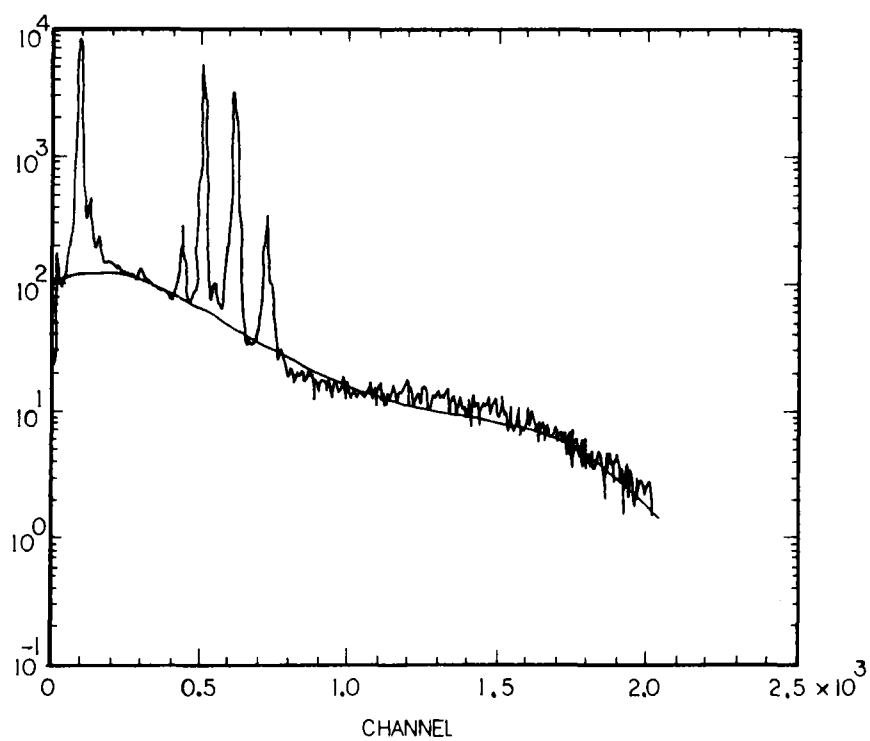


Figure 3.12 Background removal and peak fitting analysis

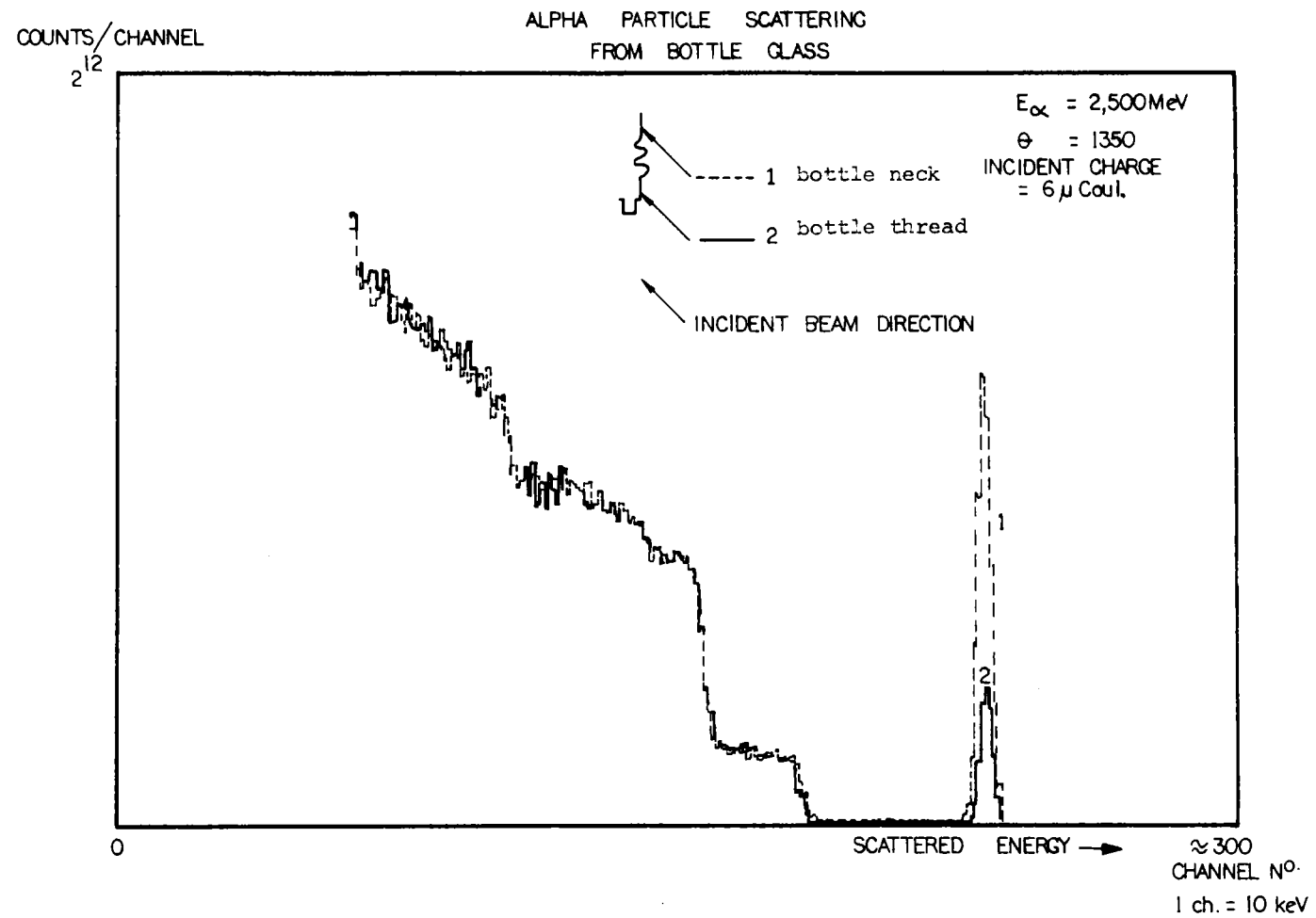


Figure 3.13 Tin concentrations on glass as indicated by backscattered alpha particle spectra

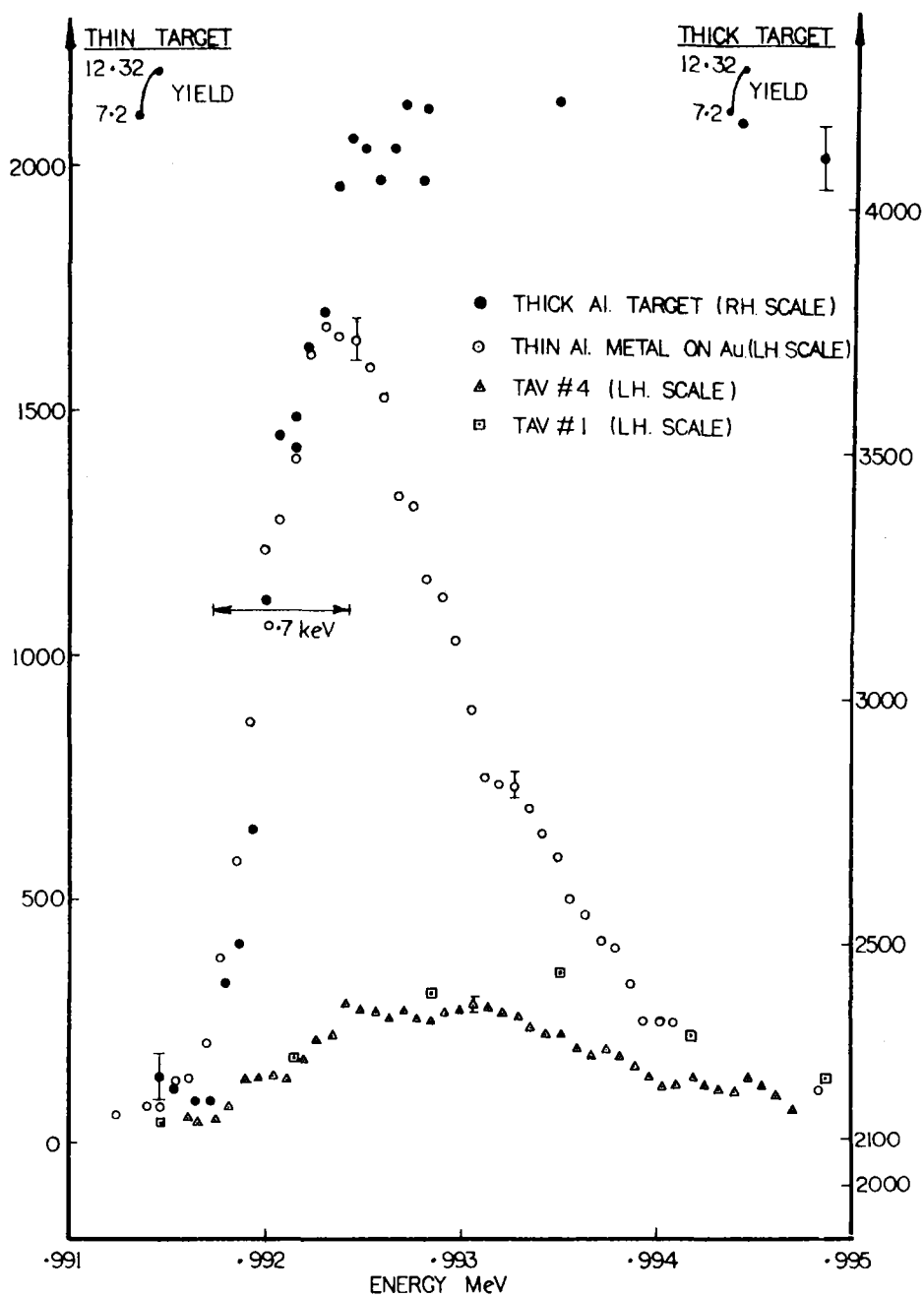


Fig. 3.14 Yield of $^{27}\text{Al}(p,\gamma)^{28}\text{Si}$ reaction as a function of proton energy (and hence depth) for thick aluminium (\bullet), an evaporated layer of aluminium on silica (\circ) and for diffused alumina layers in silica (\blacktriangle, \square)

techniques to neutralise the charging effect of the incident beam reproducible results were obtained for the shape of the 992 keV resonance in the reaction $^{27}\text{Al}(p,\gamma)^{28}\text{Si}$. Results are shown in Figure 3.14 for a thick aluminium, thin aluminium evaporated on to gold and two silica gettering samples. A large Ge(Li) detector was used to detect gamma rays in the range 7-11 MeV during the irradiation of each sample with 50 nA of protons. No detectable resonance yield was observed for a clean silica sample or a sample exposed to undoped germanium. However, the two samples used to getter aluminium doped germanium show a layer of aluminium oxide of thickness of the order of 5 μm and significantly greater than the 2 μm depth resolution of the measurements.

3.4.6 Oxygen (L. H. Russell, S. Kannard*)

Measurements have been made of ^{18}O diffusion profiles for H. de Bruin (Flinders University). Enriched ^{18}O was diffused into discs of urania and the $^{18}\text{O}(p,\alpha)^{15}\text{N}$ reaction used to obtain a depth profile from the alpha particle energy spectrum. Thick zirconium oxide and thick enriched zirconium oxide on zirconium were used as reference samples. A proton beam current of 0.8 μA was used and this was sufficient to heat the samples so that a faint red glow could be seen. At this beam current, run durations of 5-10 minutes gave sufficient counts on the diffused samples.

3.4.7 Surface fluorine layers (L. H. Russell)

The build-up of surface fluorine has been monitored for Chemical Technology Division using the well known prompt gamma ray technique. Measurements are made routinely of the variation across surfaces of fluorine on samples subject to various treatments.

3.4.8 Minibeam (A. van Heugten, M. D. Scott, L. H. Russell)

Beam diameters down to 40 μm are produced by collimation with an aperture mounted at the entrance to the sample chamber (so as to minimise divergence between aperture and sample). A specially constructed stage mounted in the chamber provides two-dimensional movement of the sample from micrometer heads which operate rods sliding through vacuum seals. A microscope is mounted in a re-entrant tube so that features of interest can be positioned during irradiation and adjusted as required.

3.4.9 Gamma ray catalogue (J. R. Bird, L. H. Russell, M. D. Scott, M. J. Kenny)

Increasing use is being made of prompt gamma rays from nuclear reactions for analytical purposes. However, there is no convenient catalogue of gamma ray energies and intensities from charged particle induced reactions for use in such work. Using papers describing charged particle beam analysis, a table of gamma rays has been prepared in order of energy, including only such gamma rays as have been used for sample analysis. Measurements have been made of the intensity of gamma rays emitted at 135° from a number of thick targets of pure elements irradiated with protons at 2 and 2.5 MeV. The results are given in Table 3.8, together with other published data. This work was reported at the Third International Conference on Ion Beam Analysis, Washington, July 1977.

3.4.10 Bibliography (J. R. Bird, B.L. Campbell[†], R. J. Cawley)

The bibliography of papers on prompt nuclear analysis has now been extended to include papers published up to the end of 1976. It contains over 1300 references, approximately half of which are concerned with backscattering techniques and the other half with nuclear reaction techniques. A computer file has been established, together with sorting and search routines which permit use of the bibliography to obtain lists of references on the use of a specific reaction or lists selected on any other key-words or parameters contained in the file.

*Australian Institute of Nuclear Science and Engineering

[†]Isotopes Division

TABLE 3.8
PROTON INDUCED GAMMA RAYS: THICK SAMPLE YIELDS

El.	E_p (MeV) E_γ	Measured Yield (γ 's/st μ C)				Yield Curve Refs.
		2.000 This work: 135°	2.500	2.000 Refs. 3-7: 90°	2.500	
Li	14-18					2)
Be	0.416	4×10^2	8×10^2			
	0.717	3.9×10^3	5.0×10^3			
	1.021	5×10^2	1.5×10^3			
	7.5					2)
B	0.430	1.0×10^6	2.5×10^6			
	0.717	2.7×10^4	1.5×10^5			
	4.439					2)
	11-17					2)
C	2.360, 9.18					2)
F	6.13					2)
Na	0.439	1.2×10^6	3.3×10^6	1.4×10^7	4.7×10^7	3)
	1.368					
	1.630	2.8×10^5	1.6×10^6			
Mg	0.390	3.7×10^3	3.2×10^4	3.3×10^3		
	0.586	3.0×10^4	9.6×10^4	3.5×10^4	1×10^5	6)
	0.843	-	7×10^2			
	0.976	4.1×10^3	3.9×10^4	4.8×10^3		
	1.013	-	1×10^3			
	1.368	-	2.1×10^5	541		
Al	0.170	1.0×10^3	1.1×10^4			
	0.843	2.5×10^4	1.9×10^5	2.6×10^4	2.3×10^5	4)
	1.013	3.7×10^4	3.8×10^5	4.0×10^4	4.5×10^5	4)
	1.368	1.0×10^4	5.1×10^4	9.8×10^3	5.6×10^4	4)
	1.778	5.4×10^3	8.2×10^3	6.4×10^3	1.1×10^4	4)
	2.836	5×10^2	1×10^3			
Si	1.273					
	1.778		3×10^2			
P	1.266			1.0×10^3	7.4×10^4	5)
	1.778			173	3.3×10^3	5)
	2.237			1.8×10^3	3.4×10^3	5)
Cl	0.568				2.5×10^3	
	0.602				7.2×10^3	
	0.697				5.5×10^3	
	1.219				1.1×10^4	7)
	1.643				1.9×10^3	7)
	1.972				1.4×10^3	7)
	2.128				3.4×10^3	7)
	2.168				3.2×10^3	7)
	2.209				0.6×10^3	

4. THEORETICAL PHYSICS

4.1 AUS Modular Scheme (J. Barry*, J. Pollard, G. Robinson)

Further verification was carried out on the AUS suite of modules. A 3-dimensional diffusion module, POW3D, is being developed and will eventually replace the present 2-dimensional module POW.

4.1.1 AUS module POW3D (J. Barry, J. Pollard)

POW3D is a 3-dimensional (x,y,z) diffusion theory module which uses a finite difference approximation to the group neutron diffusion equation. Later kinetics aspects will be added.

An important feature of the module is the selective use of different methods for solution of the basic linear equations. A method of implicit non-stationary iteration, MINI, has been developed which has potential advantages for speeding up the calculation compared with the well established successive line over-relaxation, SLOR, technique. MINI involves more calculation per solution point than SLOR, but generally requires about 20% fewer iterations to achieve convergence. This saving in a number of iterations is to be exploited in POW3D for 3-dimensional calculations involving extensive disk input-output. Present experience confirms a saving of machine time when using MINI compared with SLOR.

With any 3-dimensional module, fast input-output is an important consideration. An easy to use input-output routine has been developed which uses the available core storage for semi-permanent buffers with direct access disk storage used for any overflow. The routine simulates 'virtual storage', although possible retention in core is under control of the user rather than on the basis of ad hoc rules. Present limited experience shows a reasonable time saving in both central processing unit (CPU) time and real time when a job is run in a bigger region of machine core storage on the AAEC IBM 360/65 computer.

4.1.2 Collision probability methods (G. Robinson)

The correct representation of square or hexagonal boundaries in rod arrays is of some importance, particularly in resonance calculations. The use of a white circular boundary can introduce errors of up to 2% in resonance capture in water cooled systems. An approximate representation of the boundary shape which was based on the work of Bonalumi (1965)¹ has been included in a set of fast collision probability routines for rod arrays and clusters which have been incorporated in the MIRANDA and ICPP modules.

4.1.3 Calculation of fast reactor benchmark experiments (G. Robinson)

Calculations of a set of fast reactor critical experiments have been undertaken to check the accuracy of the representation of fast reactor nuclides in the AUS/ENDFB library. This library has groups of 0.25 lethargy width above 10 eV and includes a subgroup representation of the resonance scatterers Na, Al, Cr, Fe, Ni and Cu, as well as the fuel nuclides. All data used was taken from the ENDF/B-IV cross section library.

Details of the experiments were taken from the compilation of benchmark specifications given in ENDF-202. Homogeneous spherical models were used throughout. Calculations were made at a number of laboratories using ENDF/B-IV data and these specifications have been reported in ENDF-230. This gives the opportunity of comparing both with experiment and alternative calculations using the same cross section data. Misprints in the specifications for the assemblies VERA-1B, ZPR-6-7, ZPR-3-56B and ZPR-6-6A in ENDF-202 were noted and corrected.

*Applied Mathematics and Computing Division

¹Bonalumi, R. (1965) - Energia Nucleare, 12, 1

The modules used in the calculation were MIRANDA to prepare shielded 0.5 lethargy width group cross sections and either ANAUSN or POW to perform the spatial calculation.

Preliminary results for criticality are given in Table 4.1. As well as the deviation from experiment, there are large discrepancies between the results from various laboratories. Because the spatial calculation methods have been standardised, the inter-laboratory discrepancies should be related to the cross section preparation methods. The calculations performed at the Argonne National Laboratory employed fine-group cross sections and should be the most accurate. In general, the values of k_{eff} obtained in this study are higher than ANL results and lower than the remainder.

TABLE 4.1
FAST REACTOR BENCHMARK CRITICALITY

Benchmark	k_{eff} AAEC	k_{eff} (laboratory - AAEC) %							
		ANL	BNL	GAC	GE	HEDL	LASL	ORNL	W
VERA-11A	0.9857	-0.04				+0.28	+0.54		
ZEBRA-3	0.9931	+0.16			+2.29	+0.69			+1.12
SNEAK-7A	0.9988				+0.32	+0.18			
SNEAK-7B	0.9939				+0.08	+0.07			
ZPR-3-48	0.9965	+0.04	+0.54	+0.94	+0.47	+0.67			
ZPR-3-56B	0.9806				+1.17	+0.95		+0.43	
ZPR-6-7	0.9893	-0.43	+0.22	+1.01	+0.16	+0.45	+0.17	-0.08	-0.23
ZPPR-2	0.9894	-0.18		+1.60	+0.41	+0.79			+0.02
ZPR-3-6F	1.0095		+0.24			+0.45			
VERA-1B	0.9984		+0.03			-0.11			
ZPR-3-12	1.0046					+0.18			
ZPR-3-11	1.0052	-0.29				+0.61	+0.97	+0.28	
ZEBRA-2	0.9954	-0.77				+0.17			
ZPR-6-6A	0.9934	-0.88				+0.46	+0.25	+0.52	+0.25

4.2 Radiation Shielding

4.2.1 Bilinear vs. linear weighting of multigroup cross sections (I. Donnelly)

Neutron cross sections suitable for shielding calculations are generally available in a fine group format. It is frequently necessary to condense them into a coarse group set prior to their use in a transport theory calculation. Usually an appropriate flux spectrum is used to weight the cross sections during condensation; however a perturbation theory analysis indicated that a bilinear weighting using appropriate flux and adjoint flux spectra should result in coarse group cross sections which allow a more accurate calculation of the desired reaction rate. For example, a coarse group cross section set suitable for the calculation of neutron dose rates could be obtained by a bilinear condensation of the fine group cross sections using the infinite homogeneous flux spectrum obtained with the appropriate source term and the infinite homogeneous adjoint flux spectrum obtained with the dose rate cross section as the source term. Several numerical experiments have been carried out to test the efficacy of bilinear weighting. It was found that bilinear weighting gives excellent results if good weighting spectra have been used, but linear weighting is often more accurate when the weighting spectra are poor.

4.2.2 Commissioning of DOT code (B. McGregor)

Version 3.5 of this two-dimensional transport code has been commissioned. Significant differences were found between results obtained by DOT and the Monte Carlo code MORSE, when both were used to calculate a homogeneous problem derived from a bore hole logging study of a californium source in saturated sand. DOT allows the code user to specify various options for calculating the angular neutron fluxes transmitted across each mesh point, the two standard options being known as linear and step function solutions. DOT 3.5 allows the option of a weighted mixture of these solutions and further study showed that the use of this new option was producing incorrect results on the problem being investigated. Use of the standard options produced results more in agreement with MORSE. The results of this study have been forwarded to the code authors.

4.2.3 Overburden over ores (B. McGregor)

The gamma ray spectrum at the ground surface from an ore body at depth has an energy distribution that is dependent on (a) the radionuclides in the ground and (b) the interaction of the gamma rays emitted by these radionuclides with the ground matrix. This interaction is dominated by Compton scattering above 200 keV which is the energy range for most conventional geophysical field work. Compton scattering results in a continuous energy distribution showing less and less structure as the overburden thickness increases.

An experimental study of the effect of barren overburden by CSIRO Division of Mineral Physics consisted of measuring the gamma ray spectrum above a tank with varying depths of water, representing overburden, covering bags of uranium and thorium ore. Energy windows can be chosen into which no gamma rays are emitted by the source. These experiments showed that knowledge of the ratio of counts in such an energy window to the total count may be used to correct the total counting rate for the shielding effect of the overburden.

The results of published moments method calculations were used to calculate the theoretical spectra and these were folded with published response functions for the NaI detector. Theoretical spectra were calculated assuming a monodirectional source to approximate the experiment. The calculated responses showed agreement for the changes with overburden. Calculations were also used to evaluate the effects of ore thickness as well as overburden

thickness and to determine sensitivity limits on the correction factors.

In a field situation, the source would probably be approximately infinite in extent. Calculations assuming this isotropic source condition have been compared to published spectrum measurements made above calibration pads at the Danish RISO Research Establishment with good agreement. The work was presented at a recent International Geophysical Conference in Sydney.

4.2.4 Neutron and gamma ray flux levels around SILOE (I. Donnelly, B. McGregor)

The neutron and gamma ray flux levels in the water and concrete surrounding a D₂O reflected SILOE core have been calculated for a spherical model of the reactor core and surroundings. The fluxes obtained from the SABINE code using this model, approximate the values at the level of the core mid-plane.

A low dose rate was found outside the concrete shield indicating an over-design of the bulk shield. It may well be that a significant flux component streams through the beam tubes.

Similar calculations have been performed for the bulk shielding on HIFAR.

4.2.5 Safe calculations (B. McGregor)

An investigation was made of the possible effect of the absence of a cadmium layer from fissile material safes in the Nuclear Materials Fabrication building. The layer was intended to reduce, or even cancel out the interaction between safes which might result in the assembly of a critical array. A number of arrays of possible cell loadings were examined. As might be expected, the effect on total multiplication factor of removing the cadmium was greatest for those systems where total k_{eff} is low and many neutrons can leak out of each unit of the array. On the contrary for systems in which the individual cells are nearly critical on their own, removal of the cadmium layer produced smaller increases in the multiplication factor.

As part of the study a recommendation was made that the total moderator mass limit be 15 kg for each cell.

4.3 Reactor Data

4.3.1 Fission product cross section library (J. L. Cook, E. K. Rose, H. D. Ferguson)

The basic data for 192 fission product isotopes has been revised, with particular emphasis on the 104 nuclides whose cross sections are not contained in the ENDF/B libraries. Two methods of interpolating level spacings from experimental to unmeasured values have been investigated. The first was a revision of the Gilbert-Cameron theory fitted to experimental data to obtain values for the shell and pairing corrections. Estimates were made of errors to be expected when using the theory to interpolate to unmeasured nuclides and these, in general, were quite large, values of 50-100% or so being common. The second method used was to calculate pairing corrections using known empirical fits to mass formulae and then to calculate the correlation between the level density parameter 'a' and the Myers-Swiatecki shell corrections. A strong correlation was found only within about three units of charge or neutron number to the shell model magic numbers. Outside this range the scattering of the experimental values for 'a' around the estimated value was greater on average than three standard deviations for twenty-one nuclei. It was therefore concluded that for the 83 isotopes satisfying the above condition, reliable predictions could be made in their vicinity in the periodic table, but for the rest, the uncertainties would be too large to permit reliable estimates of statistical region cross sections.

More success was obtained in fitting the experimental values by dividing the mass range into five regions and fitting the level density parameter separately in each region, but some 20 nuclei still showed large discrepancies.

Strength function data was obtained from the Musgrove file and intermediate values needed were estimated by interpolation in charge and neutron number. Radiation widths were taken from a wide range of sources and unknown values estimated by various empirical interpolative formulae. Musgrove's interpolative formula gave acceptable results, except where spin and parity effects are large. With this data, a 104 nuclide parameter library was prepared ready for use with the new GUNYA Monte Carlo program which uses a combination of ENDF/B cross section files and predicted statistical resonance parameters to generate radiative capture and scattering cross sections which match the measured thermal cross sections and capture resonance integrals. It was found that except for ^{135}Xe , ^{149}Sm and ^{148}Pm the cross sections for unstable isotopes are associated with low yields from fission, so in many cases a large error in the predicted cross section can be tolerated in reactor physics calculations.

4.3.2 Calculation of average reaction cross sections (W. K. Bertram)

It has long been recognised that the Hauser-Feshbach theory for average reaction cross sections is inadequate in many cases. Ever since the attempt by Moldauer in 1964 to improve upon the Hauser-Feshbach theory, attempts have been made to derive a more general statistical theory from resonance theories. Even so, the Hauser-Feshbach theory is still widely used today, even though its results are suspect in many cases to which it has been applied.

It has been previously shown that a more general statistical theory can be obtained when there are only two reaction channels open. The problem for non-fluctuating, picket fence model S-matrices when the number of channels is greater than two has now been solved. By generalising these results to the case where the S-matrix widths do fluctuate, a formula for evaluating average cross sections has been obtained. Using computer generated data, comparison between this formula and the Hauser Feshbach formula has shown that the new formula provides a much more accurate description of average cross sections, especially when the number of channels is small. The method is particularly successful in evaluating cross section ratios which cannot be obtained accurately from the Hauser-Feshbach theory.

At present investigations are being conducted into the effects of direct reactions on the average cross sections and into the calculation of cross section fluctuations. A computer program is being prepared for the analysis of inelastic scattering and fission cross sections.

4.3.3 Resonance parameter analysis (B. E. Clancy, J. L. Cook, E. K. Rose)

In various compilations of the resonance parameters for ^{235}U , there are overall 26 levels identified as belonging to the $J^\pi = 3^-$ state and 40 levels belonging to the $J^\pi = 4^-$ state. Calculations of the fission cross section from 10 keV to 1.5 MeV require that there be one dominant fission channel appreciably open in each state at low energies. On the other hand, examinations of the statistics for the fission widths in each state imply that one channel is certainly open for the 3^- state, but that apparently three channels are open for $J^\pi = 4^-$. A numerical experiment was performed by supposing that small fission widths are missed by resonances being unresolved from the background noise level, and then the effective number of channels was estimated. It was found that if all widths are missed for fission widths less than one half the mean fission width, the maximum effective number of channels open in the $J^\pi = 4^-$ state could not be greater than 2.6, whereas the experiments gave a value of 3.7.

To support these findings, an expression was developed for the resolution probability of a resonance as a function of its fission width and then by fitting the mean and variance of the experimental width distribution, obtained the results shown in Table 4.2. Only for three channels open does the percentage number of levels missed for $J^\pi = 4^-$ approximate that for $J^\pi = 3^-$.

TABLE 4.2
THEORETICAL ESTIMATE OF LEVELS MISSED

J^π	No. of Channels	No. of Levels	No. of Levels Missed
3^-	1	26	3
4^-	1	40	89
4^-	2	40	48
4^-	3	40	6

In anticipation of new results measured by Keyworth et al. two methods were tested for finding the effective number of channels open, given a measured set of fission widths. The first was by attempting to calculate the partial average fission width in each channel using calculated first, second, third, etc. moments of the experimental distribution. Trial fission widths were generated by a Monte Carlo method for one, two and three channel open. After finding that errors in partial average widths could reach 100% for 20-40 levels, and that only for as many as 1000 trials did the errors become as low as 10%, it was concluded that the method of moments is unreliable for the available information.

The second method was by carrying out Pearson's χ^2 test on a subdivision of groups of the distribution. The errors were much less than those obtained by the method of moments, being from 5-10%.

4.4 Other Items

4.4.1 Detector calculations (E. Clayton)

A variety of neutron detection efficiencies have been calculated by Monte Carlo code for the organic detectors NE102 and NE213. A modified version of the code was used to provide neutron angular distribution data for multiple scattering and carbon scattering corrections for hydrogen scattering experiments at the Australian National University. Measurements made at ANU showed that although the code provided accurate efficiency data, there were minor discrepancies in the shape of the response function at high neutron energies. These discrepancies arise because of uncertainty in the relationship between deposited energy and pulse height. This question is still under investigation. Modified carbon response data improved the agreement between theory and measurement at high energies.

A gamma ray code using much of the original Monte Carlo code was developed to test gamma ray source calibrations for organic detectors. This predicted the position of the Compton edge accurately when compared to measured response functions, but overestimated the peak to valley ratio for Compton scattering except at low energies.

4.4.2 Magnetohydrodynamics and topping cycles (D. W. Lang)

At present electrical generation by combustion appears thermodynamically inefficient. One limitation is given by the temperatures at which materials making up turbine blades fail. In a number of countries attempts are being made to get economical direct conversion of gas motion into electric power. The combustion gas itself is produced at a high enough temperature to be electrically conducting and direct current is obtained when it is forced through a magnetic field.

The economics of operating a MHD duct require that the gases be conducting and therefore hot, close to the walls. With coal as a source of the combustion gas there can be a considerable slag component and the endurance of the wall becomes an important economic consideration. A number of proposals have included an alternating magnetic field so that there are no electrodes, power is obtained by induction and the temperature close to the wall can be decreased. So far there has been a consequent difficulty that the varying magnetic field has been associated with a hysteresis loss and overall the electrical energy output has been negative.

In order to remove electrodes from a MHD duct and at the same time avoid hysteresis loss, it is suggested that the magnetic field be provided by a rotor and be fixed with respect to the rotor. The magnetic field is given a spiral structure and acts as the blades of a primitive turbine. The energy is collected from the gas to produce rotation of a shaft leading to a.c. generation.

Calculations of the effects expected have been made. A small scale model suffers because torque is proportional to duct volume. It is reasonable to overcome this defect using mercury as the conducting fluid in a model.

4.4.3 Inverse reaction problem (E. Clayton, D. W. Lang, J. L. Cook)

A standard method of obtaining information about a two-body force involves the measuring of scattering cross sections. It is known that the scattering alone does not define the radial dependence of the force. The situation resembles that in X-ray diffraction analysis of crystal structure, where the pattern of scattered photons conveys the information about molecular structure. In the case of scattered particles, the scattering cross section angular distribution is divided into partial angular momentum states and the partial wave amplitudes are expressed in terms of phase shift. Each phase shift defines a whole class of phase-equivalent potentials and we attempted to define properties of this class.

The problem of finding all equivalent potentials was reduced to that of finding all orthogonal matrices that transform non-interacting wave functions into interacting ones, by means of these orthogonal matrices. All such matrices must have the same leading column and the construction of all such matrices has been demonstrated. These are to be tested in computer studies of reconstructing measured phase shifts from the defined class of potentials.

To apply these methods to measured data, the pion-nucleon system is being examined using new data. The class of non-local potentials in the seven most prominent angular momentum states are to be evaluated, and transformations between phase equivalent potentials are to be investigated.

4.4.4 Applications of unfolding techniques (D. W. Lang)

An earlier program (AAEC/PR40-P, section 4.4) written to unfold a spectrum from data (with the condition that the response matrix is experimentally measured) has been fully revised and a response function matrix is now being assembled. Smoothing of the response functions is likely to be critical in the success of the unfolding technique and several options for smoothing have been incorporated.

4.4.5 Flux spectrum unfolding (J. L. Cook, H. D. Ferguson)

The new constrained linear least squares program for obtaining neutron flux spectra from measured activation reaction rates was further tested to see if deficiencies, present in other methods, occurred. One particular feature that was a problem with our earlier theories was that the calculated group flux often reflected structure in the vicinity of resonances in the detector cross sections. In particular, an IAEA test problem, known to be the measured activations in a fast reactor spectrum, gave a dip in the flux in the neighbourhood of the 2 keV

resonance in ^{23}Na , which was one of the detecting nuclides. The unfolded spectrum obtained by omitting the ^{23}Na detector data, produced almost no change in the size of the dip, indicating the presence of a large amount of sodium absorber in the reactor.

Further work continued on the search for suitable thermal flux detectors. Natural erbium, with several resonances around 0.5 eV and a non- $1/v$ cross section over most of the thermal region, is one candidate. Such behaviour is required because the thermal flux rises to a maximum below about 0.25 eV and such a rising flux cannot be obtained from a linear combination of ' $1/v$ ' cross sections.

4.4.6 Interactive computing methods (B. E. Clancy)

In many scientific computing installations, a substantial number of the jobs submitted are small FORTRAN compile, link and run jobs, designed to test out new ideas or to perform relatively straightforward calculations. Even when conceptually simple, these jobs are not free from programming mistakes and the job may need to be revised and resubmitted several times before the 'successful-definitive' run is made. Monitoring the execution of these runs and modifying program and/or data between runs is often best done in one interactive session at a computer terminal and machine manufacturers have provided systems - such as the IBM TSO system - to allow this to be done.

Being designed to support many users simultaneously, the TSO system makes large demands on computer core storage and has not been implemented at the Research Establishment. To provide most of these facilities to a single user at one time, an interactive program package - COMFORT - has been developed to run under the normal operating system to which COMFORT looks like an ordinary batch job.

The heart of COMFORT is the control segment which interacts with the user allowing him to enter, edit and modify his FORTRAN program and data as well as to save or recover his program held in a disk library. When appropriate, this control program activates a FORTRAN compiler and then passes control to the compiled user's program. A comprehensive set of subroutines and functions is available to the control segment and linkage to these from the user's program is made at compilation time. A complete error monitor is available and, when necessary, this will regain control from the user's program and return to the control segment without aborting the user's session at the terminal.

4.5 Energy Systems Analysis

4.5.1 Australian energy data file (P. Essam*, J. Faulkner*, K. J. Maher, K.J. Stocks*)

The file now contains a number of time series relating to the Australian energy system and collated from official sources. Series are compiled for each state and the Northern Territory and are for financial years from 1947/48 unless otherwise specified. Currently, the file contains:

(1) Electricity

- (i) Primary energy consumed in power stations by fuel type (volumetric and energy units).
- (ii) Electricity produced by power stations.
- (iii) Electricity consumed by residential, commercial and industrial sector.

*Energy Systems Analysis Group, Power and Energy Program

(2) Coal

- (i) Production, stocks and consumption of black and brown coal (volumetric and energy units).
- (ii) Exports of black coal (volumetric units).

(3) Petroleum Products

- (i) Consumption of 13 major petroleum products, monthly values (volumetric units).
- (ii) National refinery production, exports and imports of 16 major petroleum products (volumetric units).

(4) Economic and Demographic Series

- (i) Populations.
- (ii) National GDP at current prices and GDP implicit price deflators.

Statistics on town gas production and consumption by states and primary energy input to gas plants by fuel type, as well as natural gas production and consumption statistics, are presently being collated.

4.5.2 Australian usage of low grade heat to 200°C (K. J. Maher, P. Essam, K. J. Stocks)

In national energy accounting the temperature at which heat is delivered to the various end-uses (steel making, domestic space heat, etc.) is as important as the quantity of energy delivered. Yet it is totally neglected in official statistics. An assessment has been made of the percentage of primary energy ultimately serving an end-use in the range -30°C to 200°C. One may anticipate increasing solar energy contributions in this range.

It is estimated that by the year 2000, 23% of Australian primary energy may ultimately be directed to refrigeration and low grade heat (LGH). Most of this energy will be in the form of coal converted to electricity serving refrigeration and LGH applications. The percentage of final use energy going to LGH would be about 16%. These estimates are 'soft' being based firstly on one of many feasible energy sector growth projections, one which assumed continued shifts to electricity in the commercial and domestic sectors and, secondly, on considerable guesswork in the LGH requirements of various sectors of the economy.

Several scenarios were postulated for the market penetration of direct solar devices serving this temperature range. With vigorous artificial incentives in a context of rapidly increasing fossil fuel prices (including Australian black coal), about 6% of final use energy could be provided in the year 2000 by solar energy. About 40% of all homes and 30% of all commercial establishments would derive all space heat/cooling and water heat from solar without conventional backup (or larger percentages with backup) and a large fraction of the food processing and wood and paper industries would run on solar process heat. A cumulative investment of about \$12 x 10⁹ (1976 dollars) in collectors would be required. With market forces alone acting, about 2% of final use energy in the year 2000 might be provided by solar. Electricity produced by photovoltaics in other than remote locations and solar ethanol could add to these contributions, but it is considered unlikely that they would do so by 2000.

5. RUM JUNGLE ENVIRONMENTAL STUDIES (B. Clancy, I. Ritchie, J. Daniel)

5.1 Field Measurements of Rainfall and Run-off

Measurements of the quantity and quality of run-off water and rainfall on White's overburden dump were continued in the 1976-77 wet season. Unfortunately, equipment problems arose and resulted in a record which contained information on only about half the total number of events.

The results confirmed the previous year's findings that the heavy metal burden of ground water is much greater than that of the run-off.

5.2 Rainfall Contribution to Ground Water

In order to relate the heavy metal burden and the magnitude of the oxidation process the soil moisture level is being monitored using a neutron scattering technique, which is non-destructive. In principle this means that the soil water content of the heap can be measured as a function of time and depth throughout the wet and dry seasons.

Six holes were drilled from the surface through to the original ground level. During the drilling program samples of soil were taken for subsequent analysis to determine the variation (if any) with depth, of sulphur and heavy metal concentrations and neutron absorption cross section. The holes were lined with end-plugged polythene tubes which were capped to stop ingress of water.

Throughout the wet season the count rate of a neutron probe was measured as a function of depth in the probe holes. Count rates from a gamma probe were also measured to determine the bulk density of the soil in the heap.

Conversion of the field measurements to density and soil water content has been less straightforward than expected and a program of laboratory measurements, backed by sophisticated neutron transport calculations, has been mounted to determine the calibration curve for the neutron probe as a function of soil density, soil water content and thermal neutron absorption cross section.

5.3 Model for Heap Leaching

The consequences were examined of assuming that the oxidation rate of pyrites in an overburden dump is determined by the rate at which the oxygen required can diffuse in from the top surface. It was shown that oxidation proceeds at a reaction front that moves away from the top surface at a rate determined entirely by the concentration of pyrites in the heap, the diffusion coefficient of oxygen in the pore space, the concentration of oxygen in the air and the ratio of the mass of oxygen to the mass of pyrites consumed in the chemical reaction describing the oxidation process.

Applied to White's overburden dump at Rum Jungle, the model indicates oxidation rates of the same order as those inferred from field measurements. It also predicts, depending on the porosity which is assumed to be between 20 and 40%, that at the present stage of the heap's development, the reaction front lies between 3 and 5 m from the surface and is advancing 7.5 to 13 cm per year. If the reaction is catalysed by iron-oxidising bacteria, then on the basis of the model, the bacterial population will be greatest in the comparatively small 'front' region, will be zero in the anaerobic region below the front and small in the upper levels of the heap.

Estimates were also made of the temperature rise at the reaction front and the temperature distribution, assuming that the only heat loss was by conduction through the soil. Heat loss to water passing through the heap could, however, be significant and a more sophisticated treatment is required.

Partly to test the predictions of the model, temperature profiles were measured in the drill holes throughout the 1976-77 wet season. These measurements show that the temperature distribution changes throughout the wet season, but that the variation differs from hole to hole. One hole shows particularly high temperatures ($\sim 53^{\circ}\text{C}$) throughout the season, while the other holes have maximum temperatures ranging from 35 to 38.5°C .

6. PUBLICATIONS6.1 Papers

- Allen, B. J., Musgrove, A. R. de L., Boldeman, J. W., Kenny, M. J. and Macklin, R. L. (1976) - Resonance neutron capture in ^{56}Fe . Nucl. Phys. A269, 408
- Allen, B. J., Musgrove, A. R. de L., Boldeman, J. W. and Macklin, R. L. (1977) - Valence neutron capture in ^{54}Fe . Nucl. Phys. A283, 37
- Allen, B. J. and Musgrove, A. R. de L. (1977) - Valence and doorway mechanisms in resonance neutron capture. Advances in Nuclear Physics (in press).
- Barrett, R. F., Bray, K. H., Allen, B. J. and Kenny, M. J. (1977) - Non-statistical effects in neutron capture γ -ray spectra. Nucl. Phys. A279, 204
- Boldeman, J. W., Fréhaut, J. and Walsh, R. L. (1976) - A reconciliation of pulsed and d.c. measurements of $\bar{\nu}_p$ for neutron induced fission of ^{235}U . Nucl. Sci. & Eng. 63, 430
- Boldeman, J. W., Allen, B. J., Musgrove, A. R. de L. and Macklin, R. L. (1977) - Resonance neutron capture in ^{89}Y . Nucl. Sci. & Eng. (in press)
- Caruana, J., Boldeman, J. W. and Walsh, R. L. (1977) - Fission fragment angular distributions for neutron fission of ^{232}Th and their interpretation with a triple-humped fission barrier. Nucl. Phys. A285, 205
- Caruana, J., Boldeman, J. W. and Walsh, R. L. (1977) - $\bar{\nu}_p$ for neutron fission of ^{232}Th near threshold. Nucl. Phys. A285, 217
- Clayton, E. J. and Derrick, G. H. (1977) - A numerical solution of wave equations for real or complex eigenvalues. Aust. J. Phys. 30, 1
- Clayton, E. J., Cook, J. L. and Rose, E. K. (1977) - Application of the inverse scattering problem to low energy pion-nucleon scattering. Aust. J. Phys. (in press)
- Kenny, M. J., Allen, B. J. and Macklin, R. L. (1977) - Resonance neutron capture in scandium below 100 keV. Aust. J. Phys. (in press).
- Kenny, M. J. and Allen, B. J. (1977) - Gamma rays from keV neutron capture in lanthanum. Aust. J. Phys.
- Musgrove, A. R. de L., Good, W. M. and Harvey, J. A. (1977) - Resonance parameters for ^{90}Zr below 300 keV. Aust. J. Phys. 30, 379.
- Musgrove, A. R. de L., Boldeman, J. W., Allen, B. J., Harvey, J. A. and Macklin, R. L. (1977) - High resolution transmission capture for ^{91}Zr . Aust. J. Phys. 30, 391
- Musgrove, A. R. de L., Allen, B. J. and Macklin, R. L. (1977) - Resonance neutron capture in ^{139}La . Aust. J. Phys. (in press)
- Trimble, G. D. and Turner, W. J. (1977) - Characteristics of two phase, one component flow with slip. Nucl. Eng. & Design 42, 287-295
- Walsh, R. L. and Boldeman, J. W. (1976) - Fine structure in the neutron emission $\nu(A)$ from ^{252}Cf spontaneous fission fragments. Nucl. Phys. A276, 189
- Whittlestone, S. (1977) - Neutron distributions from deuteron bombardment of a thick beryllium target. J. Phys. D. : Appl. Phys. 10, 1715

6.2 Reports

- Allen, B. J., Boldeman, J. W., Musgrove, A. R. de L. and Macklin, R. L. (1977) - Resonance neutron capture in the isotopes of titanium. AAEC/E402
- Allen, B. J., Musgrove, A. R. de L., Boldeman, J. W. and Macklin, R. L. (1977) - Valence neutron capture in ^{54}Fe . AAEC/E403
- Bird, J. R., Clancy, B. E. and Gemmell, W. (1977) - Alternative energy sources. AAEC/NSTB/PE17
- Clancy, B. E. (1977) - SUPERFIT - an interactive program for function evaluation and least squares fitting. AAEC/E408
- Connolly, J. W. (1977) - An analysis of self-terminating power transients in HIFAR. AAEC/E435
- Essam, P., Maher, K. J. and Stocks, K. J. (1977) - Solar energy contributions to Australian energy requirements to the year 2000, an initial appraisal. AAEC/NSTB/PE8
- Harries, J. R. and Wilson, D. J. (1977) - Measurement of the dynamic response of HIFAR. AAEC/E428
- Kenny, M. J., Allen, B. J., Musgrove, A. R. de L., Macklin, R. L. and Halperin, J. (1971) - Neutron capture by the chromium isotopes. AAEC/E400
- Lang, D. W. (1977) - Resolution unfolding with limits imposed by statistical experimental errors. AAEC/E398
- Lang, D. W. (1977) - Reactor calculations and nuclear information. AAEC/E426
- Musgrove, A. R. de L., Allen, B. J., Boldeman, J. W. and Macklin, R. L. (1977) - Non-statistical effects in the radiative capture cross sections of the Nd isotopes. AAEC/E401
- Musgrove, A. R. de L., Good, W. M. and Harvey, J. A. (1977) - Neutron resonance parameters of ^{96}Zr below 100 keV. AAEC/E415
- Rainbow, M. T., Ritchie, A. I. M. and Sullivan, L. (1977) - The calculation of angular neutron spectra from the thick Li(p,n) source. AAEC/E424
- Ritchie, A. I. M. (1977) - Heap leaching: a gas diffusion rate limited model. AAEC/E429
- Ritchie, A. I. M. (1977) - Flow and diffusion of a two species gas mixture in a porous slab. AAEC/E430
- Robinson, G. S. (1977) - AUS module MIRANDA - a data preparation code based on multi-region resonance theory. AAEC/E410
- Rose, E. K. and Cook, J. L. (1977) - An evaluation of the Gilbert-Cameron level density parameters. AAEC/E419
- Turner, W. J. and Trimble, G. D. (1977) - Blowdown and flow reversal on the IETI-1 rig. NEA-CSNI Standard Problem 3. OECD-NEA SINDOC(76)48
- Whittlestone, S. (1976) - Neutron energy spectra from the thick target Be(d,n) B reaction. AAEC/E399
- Whittlestone, S. (1977) - A time of flight measurement system using the elevated target facility for the AAEC 3 MeV Van de Graaff accelerator. AAEC/E420

6.3 Conference Papers

- Allen, B. J., Musgrove, A. R. de L. and Boldeman, J. W. (1977) - Neutron capture mechanisms in the 3s and 3p regions. 4th National Soviet Conf. on Neutron Physics, Kiev
- Bentley, K. W., Wall, T. and Wyatt, J. H. (1977) - Fission track analysis of uranium distributions in biological tissues. Australian Radiological Protection Society, Melbourne.
- Bird, J. R., Scott, M. D., Russell, L. H. and Kenny, M. J. (1977) - Analysis using ion induced gamma rays. 3rd Int. Conf. on Ion Beam Analysis, Washington.
- Boldeman, J. W. (1977) - Review of $\bar{\nu}$ for ^{252}Cf and thermal neutron fission. Proc. Int. Specialists' Meeting on Neutron Standards and Applications, Gaithersburg. (To be published)
- Caruana, J., Boldeman, J. W. and Walsh, R. L. (1977) - Fission fragment angular distributions for neutron fission of ^{232}Th and their interpretation with a triple humped fission barrier. 4th National Soviet Conf. on Neutron Physics, Kiev.
- Caruana, J., Boldeman, J. W. and Walsh, R. L. (1977) - $\bar{\nu}_p$ for neutron fission of ^{232}Th near threshold. 4th National Soviet Conf. on Neutron Physics, Kiev.
- Harries, J. R. and Wilson, D. J. (1977) - The dynamic behaviour of HIFAR. DIDO/PLUTO Users' Conf., Jülich, Sept.

- - - - -

PHYSICS DIVISION SEMINARS

The following seminars were presented by Physics Division staff during the year

1977

Feb. 3	J. W. Boldeman	Neutron Physics at Bruyères-le-Châtel
Mar. 3	K. J. Maher	Energy Management in Australia - a report on the Institute of Fuel Conference, November 1976
Mar. 17	R. L. Walsh	'La Ville Lumière - 1976' (or fission fragment kinetic energies in France)
May 12	G.R. Hogg and J. Tendys	Fusion Sketch Book
June 9	J. R. Bird	Alternative Energy Sketch Book
July 7	W. Gemmell	The Undesirable Fast Breeder - Fact or Myth?

DISTRIBUTION LIST - AAEC/PR43-P

1. Chairman
2. Deputy Chairman
3. Mr. K. A. Alder, Commissioner
4. Mr. B. J. Callinan, Commissioner
5. Professor H. Messel, Commissioner
6. Head, Nuclear Science and Technology Branch
7. Program Manager, Power and Energy
8. Program Manager, Uranium Fuel Cycle
9. Program Manager, Nuclear Science and Applications
10. Site Manager
11. Chief, Materials Division
12. Chief, Physics Division
13. Chief, Engineering Research Division
14. Chief, Chemical Technology Division
15. Chief, Isotope Division
16. Chief, Instrumentation and Control Division
17. Chief, Applied Mathematics and Computing Division
18. Chief, Mechanical Development Section
19. Head, Regulatory and External Relations Branch
20. Secretary
21. Director, Information Services
22. Library
23. Director, Nuclear Plant Safety Unit, Mascot
24. Head, Nuclear Studies Group
25. Mascot Library
26. Mr. D. J. Stevens, Director ARL
27. Controller, Site Information Services
28. Executive Officer, AINSE
- 29-31 R.E. Library
32. Washington Office
- 33-34 London Office
35. Vienna Office
36. Tokyo Office
37. Leader, Experimental Reactor Physics Section
38. Leader, Neutron Physics Section
39. Leader, Theoretical Physics Section
40. Leader, Reactor Performance Section
41. Leader, Engineering Physics Section
42. Leader, Chemical Physics Section
43. Leader, Applied Physics Section
44. Leader, Health Physics Research Section
45. Leader, Radioisotope Services Branch
46. Leader, Pharmaceutical & Chemical Products Section
47. Leader, Irradiation Research Section
48. Leader, Reactor Operations Section
- 49-89 W. Gemmell for INDC and Bilateral Agreement correspondents
90. B. Allen
91. J. Boldeman
92. J. Connolly
93. J. Cook
94. P. Duerden
95. G. Durance
96. J. Harries
97. G. Hogg
98. M. Kenny
99. D. Lang
100. B. McGregor
101. A. Musgrove
102. J. Pollard
103. M. Rainbow
104. I. Ritchie
105. J. Tendys
106. W. Turner
- 107-137 J. R. Bird (for special distribution)

DISTRIBUTION LIST (cont'd)

138. D. Byers (University of Canterbury, N.Z.)
139. V. Deniz (BARC, India)
140. S. Kapoor (BARC, India)
141. N. Veeraraghavan (BARC, India)
142. G. K. Mehta (Indian Institute of Technology)
143. S. Supadi (BATAN, Bandung)
144. I. Supki (BATAN, Bandung)
143. G. Tyror (AEEW, UK)
144. J. Askew (AEEW, UK)
145-165 Bilateral Agreements (UKAEA 5, US ERDA 11, AECL 5) via H.O.
166-176 Spares